AGU PUBLICATIONS

Geochemistry, Geophysics, Geosystems

RESEARCH ARTICLE
10.1002/2016GC006494

Key Points:
- The first multidisciplinary characterization of Secca delle Fumose, which is the largest submarine hydrothermal manifestation in the offshore sector of Campi Flegrei caldera
- A new technique to quantify the CO_2 output from submarine hydrothermal vents by systematic vertical profiling of seawater pH and pCO_2
- The CO_2 and energy (heat) outputs from the Secca delle Fumose degassing area are estimated at ~50 tons/d and ~80 MW, respectively

Supporting Information:
- Supporting Information S1
- Movie S1
- Movie S2
- Table S1
- Table S2

Correspondence to:
R. Di Napoli,
rossella.dinapoli@unipa.it

Citation:
Di Napoli, R., et al. (2016), Hydrothermal fluid venting in the offshore sector of Campi Flegrei caldera: A geochemical, geophysical, and volcanological study, *Geochem. Geophys. Geosyst.*, *17*, 4153–4178, doi:10.1002/2016GC006494.

Received 16 JUN 2016
Accepted 29 SEP 2016
Accepted article online 4 OCT 2016
Published online 27 OCT 2016

Hydrothermal fluid venting in the offshore sector of Campi Flegrei caldera: A geochemical, geophysical, and volcanological study

R. Di Napoli[1], A. Aiuppa[1,2], A. Sulli[1], S. Caliro[3], G. Chiodini[4], V. Acocella[5], G. Ciraolo[6], M.A. Di Vito[3], F. Interbartolo[1], C. Nasello[6], and M. Valenza[1]

[1]Dipartimento di Scienze della Terra e del Mare, Università di Palermo, Palermo, Italy, [2]Istituto Nazionale di Geofisica e Vulcanologia, Sezione di Palermo, Palermo, Italy, [3]Istituto Nazionale di Geofisica e Vulcanologia, Osservatorio Vesuviano, Napoli, Italy, [4]Istituto Nazionale di Geofisica e Vulcanologia, Sezione di Bologna, Bologna, Italy, [5]Dipartimento di Scienze, Università di Roma Tre, Roma, Italy, [6]Dipartimento di Ingegneria Civile, Ambientale, Aerospaziale, dei Materiali, Università di Palermo, Palermo, Italy

Abstract The ongoing unrest at the Campi Flegrei caldera (CFc) in southern Italy is prompting exploration of its poorly studied offshore sector. We report on a multidisciplinary investigation of the Secca delle Fumose (SdF), a submarine relief known since antiquity as the largest degassing structure of the offshore sector of CFc. We combined high-resolution morphobathymetric and seismostratigraphic data with onshore geological information to propose that the present-day SdF morphology and structure developed during the initial stages of the last CFc eruption at Monte Nuovo in AD 1538. We suggest that the SdF relief stands on the eastern uplifted border of a N-S-trending graben-like structure formed during the shallow emplacement of the Monte Nuovo feeding dike. We also infer that the high-angle bordering faults that generated the SdF relief now preferentially allow the ascent of hot brines (with an equilibrium temperature of 179°C), thereby sustaining hydrothermal degassing on the seafloor. Systematic vertical seawater profiling shows that hydrothermal seafloor venting generates a sizeable CO_2, pH, and temperature anomaly in the overlying seawater column. Data for the seawater vertical profile can be used to estimate the CO_2 and energy (heat) outputs from the SdF area at ~50 tons/d (~0.53 kg/s) and ~80 MW, respectively. In view of the cause-effect relationship with the Monte Nuovo eruption, and the substantial gas and energy outputs, we consider that the SdF hydrothermal system needs to be included in monitoring programs of the ongoing CFc unrest.

1. Introduction

Understanding unrest at volcanoes located in coastal areas requires exploration of both their onshore and offshore sectors. However, in spite of recent substantial advances in submarine volcano exploration [*Butterfield et al.*, 1997; *de Ronde et al.*, 2001; *Baker et al.*, 2002; *Coumou et al.*, 2008; *Lupton et al.*, 2008; *Staudigel and Clauge*, 2010; *Staudigel et al.*, 2010; *Embley et al.*, 2012; *Nomikou et al.*, 2012; *de Ronde and Stucker*, 2015], the offshore sectors of volcanoes remain less characterized than their onshore counterparts, owing to obvious technical challenges.

This is especially the case for the Campi Flegrei caldera (CFc), which is a large and historically active volcanic system along the Neapolitan Tyrrhenian coast of Italy. The morphology of the volcano (Figure 1) is today dominated by two largely submerged calderas that were produced by two high-magnitude explosive eruptions: the ~39ka Campanian Ignimbrite [*Rosi et al.*, 1996; *Marianelli et al.*, 2006; *Pappalardo et al.*, 2008] and the ~15 ka Neapolitan Yellow Tuff (NYT) [*Orsi et al.*, 1992, 1995]. The subaerial resurgent sector of the NYT caldera floor has been the focus of extensive geological work in recent decades [*Rosi et al.*, 1983; *Rosi and Sbrana*, 1987; *Orsi et al.*, 1996; *Di Vito et al.*, 1999]. In contrast, the submerged southern sector of CFc (Figure 1) has received far less attention [*Pescatore et al.*, 1984; *Bruno*, 2004], and its morphology and structure have only recently been investigated with modern high-resolution imaging tools [*Passaro et al.*, 2013; *Somma et al.*, 2016] and based on high-resolution seismostratigraphic data [*Sacchi et al.*, 2014].

The need for volcanological studies at CFc increased following the deformation and seismic unrest that started in the 1950s [*Del Gaudio et al.*, 2010], culminating in the 1982–1984 bradyseismic crisis [*Barberi et al.*,

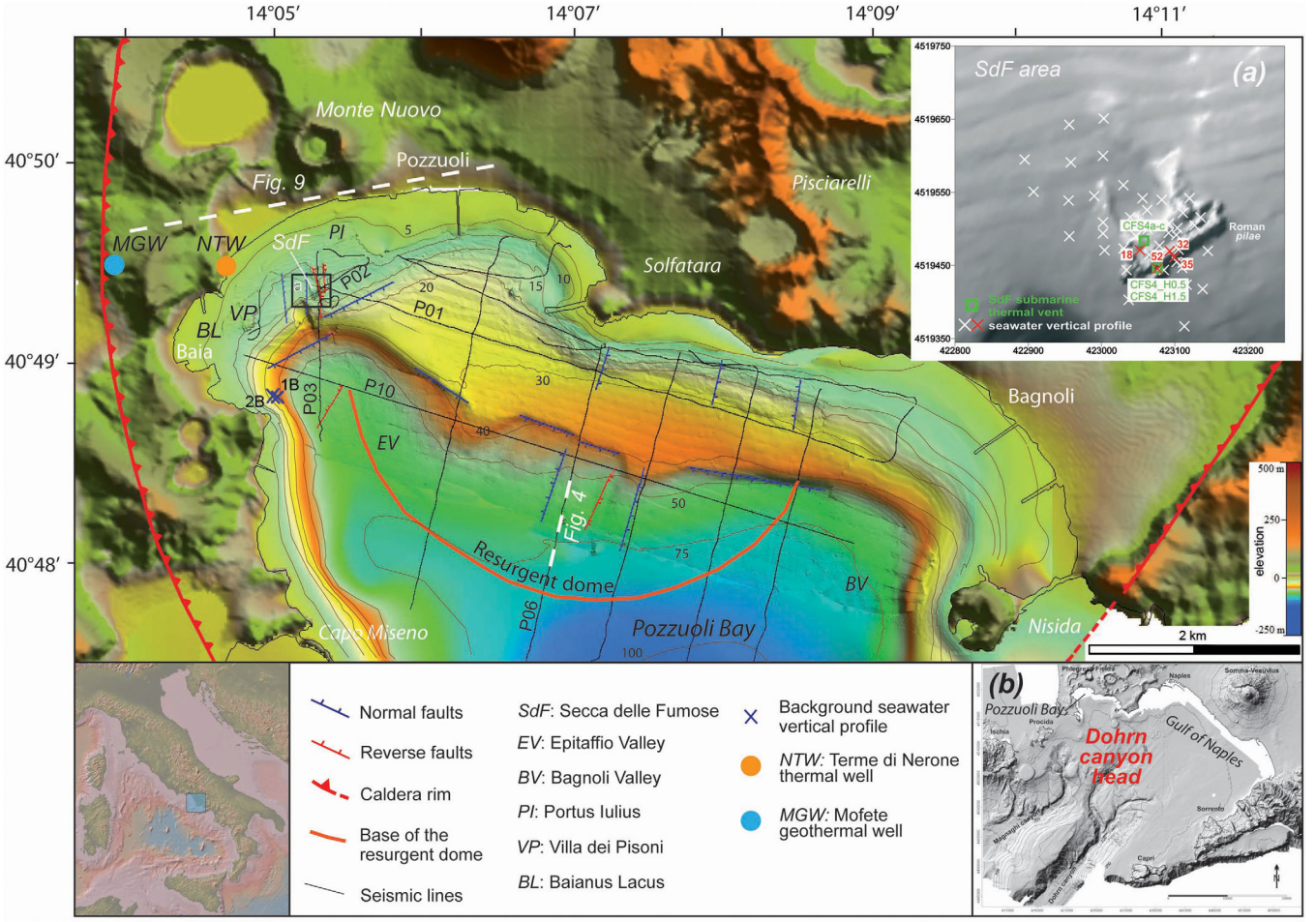

Figure 1. Morphobathymetric map of Pozzuoli Bay, obtained by processing high-resolution multibeam side-scan-sonar data, that were acquired during 3–7 October 2014. The digital elevation map of the onshore CFc sector is taken from GeoMapApp (http://www.geomapapp.org/). Normal and reverse faults were inferred from the analysis of seismic sections, while the location of the CFc resurgent dome is taken from *Sacchi et al.* [2014]. The georeferenced positions of the seismic lines are indicated by black traces. Dashed white lines mark the traces of seismic and geological cross sections illustrated in Figures 4 and 9. The empty box labeled *a* marks the location of the SdF submarine hydrothermal area detail of which is given in the top-right inset *(a)*. The crosses in this inset show the locations of the seawater vertical profiles (the red crosses were obtained with assistance from a scuba diver between the Roman pilae), while the green open squares show the locations of the directly sampled seafloor thermal vents. *(b)* Inset showing a digital map of the offshore Campanian sector illustrating the position of Pozzuoli Bay and Dohrn Canyon (modified from *Aiello et al.* [2005]).

1984; *De Natale et al.*, 2006]. This unrest, which is probably the first after several centuries of deflation [*Morhange et al.*, 2006] following the last eruption at Monte Nuovo (Figure 1) in AD 1538 [*Di Vito et al.*, 1987, 2016; *Dvorak and Gasparini*, 1991; *Piochi et al.*, 2005; *Guidoboni and Ciuccarelli*, 2011], continues today [*Chiodini et al.*, 2010, 2012, 2015], raising concerns about the possibility of the volcano reawaking.

Recent work has highlighted the role of magmatic volatiles in triggering the current (from 2005 to the present) CFc unrest [*Chiodini et al.*, 2003, 2010, 2012, 2015]. High magmatic CO_2 degassing emissions (~1600 tons/d, equal to 16.8 kg/s) have been identified in soils [*Chiodini et al.*, 2001, 2012] and fumaroles [*Aiuppa et al.*, 2013, 2015; *Pedone et al.*, 2014a] of the Solfatara-Pisciarelli hydrothermal area (Figure 1), and have been implicated as causal factors in the uplift and seismicity [*Chiodini et al.*, 2003, 2012, 2015; *Bianco et al.*, 2004; *Vanorio et al.*, 2005; *De Siena et al.*, 2010; *D'Auria et al.*, 2011, 2012]. However, it remains unknown if this unusually strong CO_2 degassing regime also extends to the submerged central sector of CFc, where both long-term deformation [*Sacchi et al.*, 2014] and short-term deformation [*Orsi et al.*, 1999] are also significant, and where hydrothermal seafloor manifestations are widespread [*Giacomelli and Scandone*, 2012, and references therein].

Here we present the results of a multidisciplinary survey aimed at characterizing the morphological, structural, and hydrothermal setting of Secca delle Fumose (SdF) (Figure 1a), which is a small submarine

relief hosting the strongest submarine thermal manifestations in the offshore sector of CFc [*Vaselli et al*., 2011; *Giacomelli and Scandone*, 2012]. This hydrothermal site is of special interest owing to its proximity to and possible genetic link with [*Guidoboni and Ciuccarelli*, 2011; *Giacomelli and Scandone*, 2012] the Monte Nuovo eruption theatre (Figure 1). We combine cutting-edge CO_2 profiling technology, direct sampling of thermal vents, geological data, multibeam data from high-resolution morphobathymetry, and seismic profiling in an attempt to derive a comprehensive model for this actively degassing structure. The first estimates of the CO_2 and energy (heat) outputs from the SdF are presented, thereby refining previous gas and energy budgets for the restless CFc [*Chiodini et al*., 2005]. Our results confirm that characterizing the offshore sectors of coastal volcanoes is crucial to fully understanding their degassing behaviors.

2. The Study Area

2.1. Pozzuoli Bay

Pozzuoli Bay (Figure 1) is a minor inlet of the Gulf of Naples in southern Italy that represents the southern submerged sector of the NYT caldera of CFc. The complex morphology of this bay reflects the interaction between sea-level oscillations, geomorphological processes, and tectonic-volcanic activity, and it is largely controlled by post-NYT asymmetric resurgence of the CFc floor [*Orsi et al*., 1996]. *Sacchi et al*. [2014] suggested that the northern offshore sector of the caldera floor has been uplifted by ∼180 m since the NYT eruption, which is approximately threefold higher than the uplift of ∼60–80 m seen onshore [*Cinque et al*., 1985; *Orsi et al*., 1996; *Di Vito et al*., 1999; *Isaia et al*., 2009]. In contrast, the southern-central sector of the bay is a poorly deformed structural depression that is being 110 m b.s.l. at its deepest point (Figure 1). The shelf edge is located off the bay, toward the S and SW, where it is incised by the head of Dohrn Canyon (Figure 1b).

The morphobathymetric data in Figure 1 show that the dome-shaped resurgent N-sector and the undeformed S-sector [*Sacchi et al*., 2014] are joined by two structural low points: Epitaffio Valley (EV) to the W and Bagnoli Valley (BV) to the E (Figure 1). EV develops in the continental shelf in a NW-SE direction, at depths of 50–90 m b.s.l., and is interrupted seaward by a NW-SE-trending ridge representing the prolongation of Capo Miseno. The BV trends NE-SW, and is a tributary of the main system.

The complex deformation history of the bay, combined with a general sea-level rise over the Holocene [*Lambeck et al*., 2011], is responsible for the presence of at least two major terraced surfaces in the continental shelf, which are at depths of 10–15 and 30–35 m b.s.l. (Figure 1). These are separated by a dipping slope from 3° to 11°, with this dip increasing toward the SE. The main terrace is located at 30–35 m b.s.l. and is tilted by 0.2° toward the SE. The presence of several Roman-period artifacts (*BL*, *VP*, *PI* in Figure 1) at a depth of ∼10 m b.s.l. [*Passaro et al*., 2013] indicate that general subsidence has occurred in the area over the last 2 ka. This subsidence [*Morhange et al*., 2006] was interrupted at least twice, in mediaeval times before the AD 1538 Monte Nuovo eruption [*Di Vito et al*., 1987; *Dvorak and Gasparini*, 1991], and from the 1950s to the present day [*Del Gaudio et al*., 2010; *Chiodini et al*., 2015].

2.2. Secca Delle Fumose

SdF is a small (∼0.14 km^2) ridge-shaped submarine relief located ∼800 m from the coast in the northwestern sector of Pozzuoli Bay (Figure 1). The SdF relief emerges from the surrounding seafloor (∼20 m b.s.l.) to reach ∼4 m b.s.l. at its highest point. High-resolution morphobathymetric data (Figure 1) [*Passaro et al*., 2013; *Somma et al*., 2016] and archaeological surveys [*Scognamiglio*, 2002; *Brandon et al*., 2008] indicate that the relief is largely anthropogenic. It consists of a dense network of square (∼10 m × 10 m) pillars ("pilae") of the Roman period (first century BC), mostly aligned along a N60°E direction [*Passaro et al*., 2013] (Figure 1a). The pilae edifice itself is enigmatic from an archaeological point of view. Located between the entry channels of two (now submerged) Roman harbors (Portus Iulius and Baianus Lacus; *PI* and *BL* in Figure 1), the structure has been variously interpreted as an ancient artificial reef or breakwater, a pier, a lighthouse, and an artificial islet house of a thermal bath [*Di Fraia*, 1993, 2011; *Scognamiglio*, 2002; *Brandon et al*., 2008]. Whatever its original use and function, the structure was later submerged (as were most Roman artifacts in the area) due to the southern NYT caldera-floor sector generally subsiding by >5 m over the past 2ka [*Passaro et al*., 2013].

SdF is particularly significant for interpreting the recent historical evolution of CFc. It lies only a few hundred meters S of the Monte Nuovo edifice (Figure 1) and, based on historical chronicles and documents, hosted the initial stages of the AD 1538 CFc eruption. According to the eruption chronology (reconstructed by *Guidoboni and Ciuccarelli* [2011] and *Giacomelli and Scandone* [2012]), SdF was part of (or immediately adjacent to) a large seafloor sector that underwent a rapid uplift (on the order of a meter) during the hours prior to the eruption onset. An eruptive fissure that opened in the same SdF area rapidly propagated rapidly away from the coast, and finally led to the eruption at Monte Nuovo [*Di Vito et al*., 1987; *Ventura et al*., 2009]. It is worth noting that the degassing and seismic activity were apparently concentrated in the Solfatara area (Figure 1) in the years prior to the AD 1538 eruption, and only became concentrated near Monte Nuovo shortly (on a timescale of days) prior to the eruption [*Guidoboni and Ciuccarelli*, 2011]. This observation confirms the necessity of extending monitoring efforts to areas other than the Solfatara area itself, which is the current epicenter of CFc unrest.

Today there are several thermal vents discharging hot (∼80°C) gas-rich hydrothermal fluids interspersed within the SdF Roman pilae (green open squares in Figure 1a). The isotope composition of the released gases (C and He) are similar to those released in the Solfatara-Pisciarelli area (Figure 1), possibly indicating a common fluid origin [*Vaselli et al*., 2011].

Quantifying the gas (i.e., CO_2) output from these manifestations and identifying their geological significance were major objectives of this study.

3. Methods

3.1. Field Operations, Data Acquisition, and Processing

The present results were obtained during two multidisciplinary surveys in Pozzuoli Bay performed in October 2014 and May 2015 and conducted within the framework of the DPC-INGV Project V2 [*Acocella and Chiodini*, 2015]. Results of earlier (unpublished) direct sampling of SdF vent fluids are also reported (section 3.1.4).

3.1.1. Morphobathymetric and Seismostratigraphic Data

Morphobathymetric and seismostratigraphic data were acquired during 3–7 October 2014 (Figure 1). Pozzuoli Bay was investigated down to depths of approximately 90 m b.s.l. We used a high-resolution multibeam echo-sounder (MBES Reson SEABAT 8125) working at 455 kHz. The transducer consists of 240 beams with a 0.5° across-track beam footprint to provide a maximum total swath width of 120°, and an along-track resolution of 1°. The acquisition parameters provided a high-resolution scan of the seafloor, with an overlay of 10–20%, with the acquisition range chosen to eliminate lateral beams and to maximize the ping rate (20–40 Hz). The acquisition system included a gyrocompass and a motion sensor so that vessel movements could be corrected in real time. Measurements were made every meter, with 217 km of lines being acquired for a total coverage of 15 km^2 (Figure 1). We used the Reson PDS 2000 acquisition software and editor tools to acquire, store, and process morphobathymetric data. A grid model with 3 m cells was obtained using the Kriging interpolation algorithm, and analyzed with the Global Mapper™ software (version 13). A test carried out to detect angular misalignments and timing differences in the multibeam system yielded a pitch of −2.6°, a roll of −0.6°, and a yaw of 3.4°, with these values used later for calibration with ad hoc lines. Two sound-velocity probes (Teledyne RESON PorTable SVP-15) were used to for continuously measure speed profiles in two zones with different bathymetry.

Morphobathymetric elements and depositional/structural features were characterized using high-resolution seismostratigraphic data obtained with a GeoChirp II system working at 1.5–13 kHz. The trigger rate was set to 4 pulses/s, with the delay and acquisition window kept constant, and the gain being varied to enable the seafloor to be search. The high-resolution chirp seismostratigraphic data were stored in SEG-Y format, and subsequently processed and interpreted with the Geosuite software. The processing sequence included spherical divergence correction, bandpass filtering (300–3000 Hz), swell filtering, traces mixing, automatic gain control, and constant gain. Signal penetration reached up to 50 ms (two-way travel time, twt), with a vertical resolution of 0.4 m at the seafloor. We acquired about 50 km of seismic lines in the NW-SE and NE-SW directions (Figure 1).

The combined interpretation of multibeam and seismostratigraphic data allowed the location and orientation of recent faults to be inferred; that is those having surface expression on the seafloor (as shown in

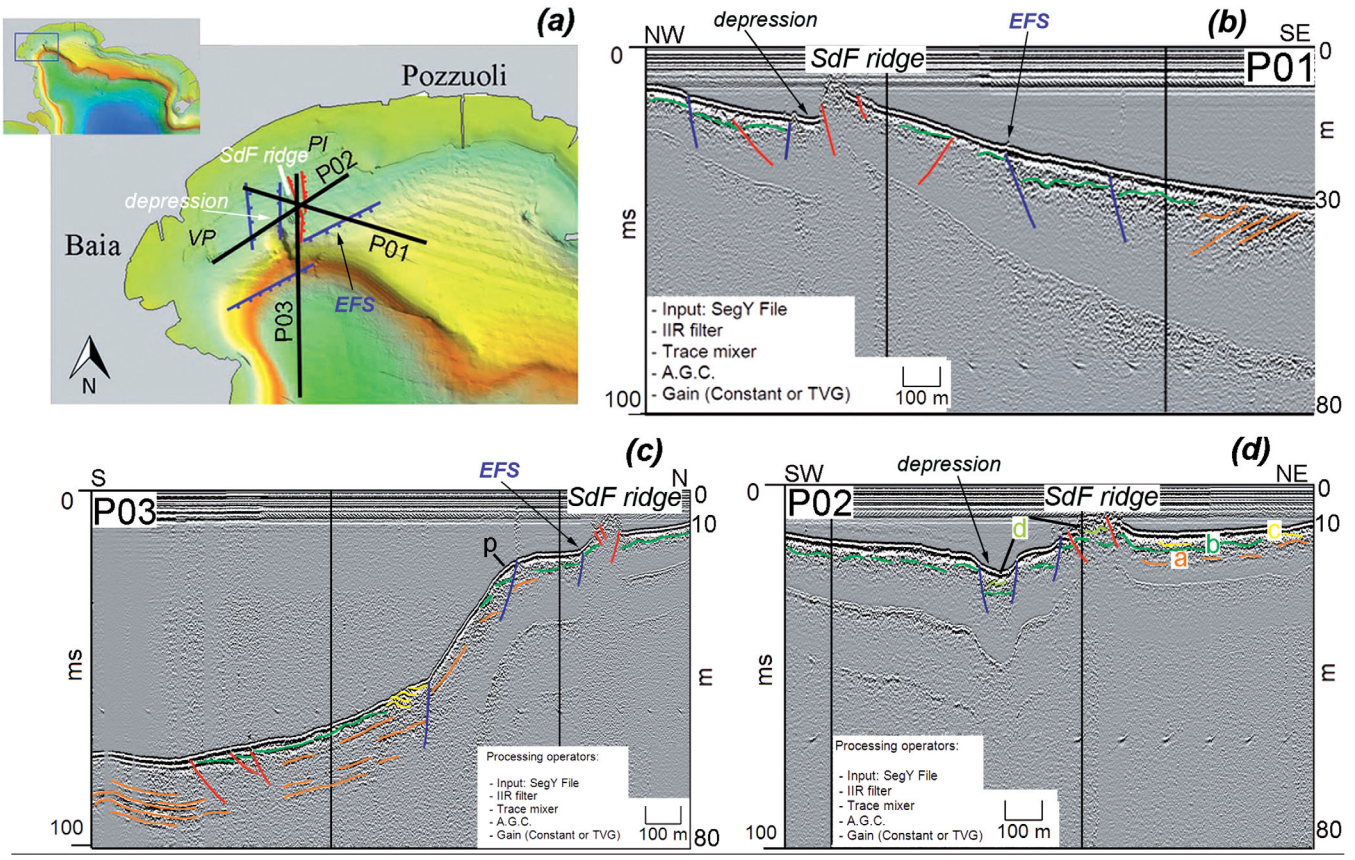

Figure 2. Seismostratigraphic cross sections intersecting the SdF area (the traces of the three sections are illustrated in the morphobathymetric map in the inset (a)). The two-way traveltimes were converted into depths using a P-wave velocity of 1600 m/s. The vertical lines are the software-generated marks of shot points. SdF appears as a ridge-shaped relief bordered by both reverse (red) and normal (blue) faults. These are identified by dislocation of individual seismic horizons on the order of a meter. The fault trends were traced based on seismostratigraphic and morphobathymetric evidence, considering they are recent faults with effects on the seafloor morphology, as well as correlations with onshore structures. *EFS*: extensional fault system (see text). Key seismic horizons (b–d) are indicated (see definition in Figure 4 and supporting information Table S2). Seismostratigraphic data identify a progradational pattern (*p* in Figure 2c) for the inner-to-outer shelf transition zone. Vertical lines in Figures 2b–2d indicate the shot points.

Figures 1–3). Each fault was initially identified in seismic profiles (Figure 2) and then the orientation (mapped in Figures (1 and 2)a, and 3a) was tracked from the pattern (orientation) of morphological features that faults produce on the seafloor, as derived from the multibeam model (Figure 1).

The interpretation of acoustic data was supported by photographic and video observations made with a VideoRay remotely operated vehicle (ROV). Supporting information Movie S1 provides an example of a high-resolution video recorded in the SdF area by the ROV using a GoPro camera.

3.1.2. Vertical Seawater Profiling

Based on the results of the explorative campaign performed in October 2014, we executed a new survey on 4 and 5 May 2015 to quantify the impact of the SdF hydrothermal seafloor vents on the overlying seawater column. We used an underwater CO_2 sensor (HydroC^{TM}, CONTROS System and Solutions, Kiel, Germany) and an Ocean Seven 303 CTD multiparameter probe (IDRONAUT) to obtain vertical profiles of pressure, salinity, temperature, pH, and CO_2 partial pressure (pCO_2) (Table 1) along the seawater column.

The HydroC sensor is a small submersible measuring system that determines the partial pressure of CO_2 in seawater (pCO_2) using a nondispersive infrared spectrometer [*Fietzek et al.*, 2014]. A semipermeable membrane (installed on the sensor headspace) allows CO_2 (and other dissolved gases) to diffuse into the internal gas equilibration space of the sensor [*Fietzek et al.*, 2014]. An external water pump ensures that seawater flows continuously to the head of the sensor and reduces the thickness of the static boundary layer in front of the membrane [*Fietzek et al.*, 2014]. Our HydroC prototype sensor is calibrated (over the temperature range of 13–30°C) to measure pCO_2 over the range of 100–6000 μatm (10–608 Pa) with a resolution of <1 μatm ($\sim$0.1 Pa). The output data (pCO_2, in μatm) were acquired at 1 Hz and visualized in real time on a PC

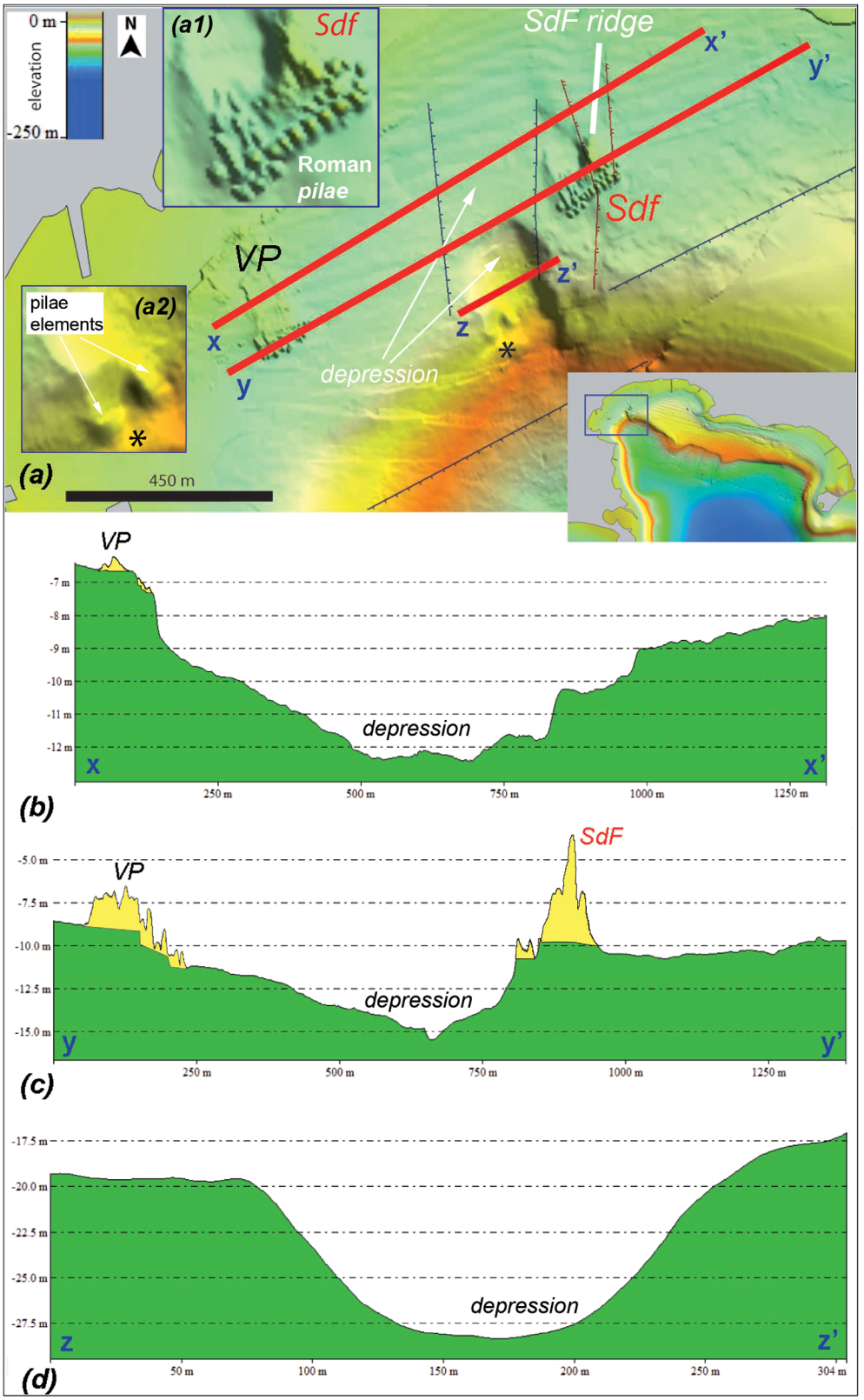

Figure 3. (a) Detailed morphobathymetric map of the SdF area. The red solid lines identify the traces of the three cross sections illustrated in (b) to (d). A N-S-oriented depression, interpreted as a graben, extends between SdF and Villa dei Pisoni (*VP*). This depression terminates in a large scarp of a landslide that is visible in cross section z-z′ (d). Yellow areas indicate the anthropogenic structures. The insets in Figure 3a are zooms of Figure 3a1 the SdF Roman structure (pilae) and Figure 3a2 of pilae elements inside the depression (see text).

Table 1. Results of Seawater Vertical Profiles Acquired in the Pozzuoli Bay[a]

Site	Date	East	North	Depth (Min/Max)	Temperature (Min/Max)	Salinity (Min/Max)	pH (Min/Max)	pCO_2 Mean (Min/Max)	Cex Mean (Min/Max)
1	5/4/2015	423030	4519560	11.6/0.6	16.8/19.1	36.8/37.5	8.18/8.32	383 (337/426)	7.6 (1.1/12.7)
2	5/4/2015	423056	4519542	11.8/0.7	16.7/18.9	36.9/37.5	8.14/8.32	405 (340/448)	8.3 (0/14.5)
3	5/4/2015	423082	4519540	6.8/0.5	17.6/19.3	36.8/37.2	8.19/8.32	361 (345/384)	8.2 (0.1/11.9)
4	5/4/2015	423120	4519542	7.7/0.2	17.5/19.2	36.8/37.3	8.22/8.32	366 (344/389)	9.3 (4/12)
7	5/4/2015	423039	4519516	12.0/0.5	17.0/20.6	36.8/37.5	8.10/8.32	449 (361/535)	10.6 (1.8/18.3)
8	5/4/2015	423062	4519526	12.6/0.5	16.8/19.5	36.9/37.6	8.06/8.32	437 (380/488)	10.3 (0/18.4)
9	5/4/2015	423091	4519506	6.8/0.5	17.8/19.6	36.8/37.2	8.17/8.33	369 (345/414)	9.8 (0.1/12.8)
10	5/4/2015	423111	4519522	5.4/0.8	18.1/19.2	36.8/37.0	8.30/8.32	345 (341/351)	9.1 (7.2/10.2)
11	5/4/2015	423135	4519516	6.5/0.3	17.9/21.1	36.8/37.1	8.26/8.32	377 (370/405)	11.7 (8/13.1)
13	5/4/2015	423047	4519490	10.1/0.3	17.5/21.9	36.4/37.4	8.09/8.32	434 (376/530)	11.9 (0/20.1)
14	5/4/2015	423063	4519500	9.6/0.6	17.4/19.4	36.9/37.5	7.97/8.32	498 (412/657)	16.7 (0/26.8)
15	5/4/2015	423092	4519495	8.7/0.6	17.7/19.3	36.9/37.4	7.77/8.32	538 (405/908)	23.5 (0/35.9)
16	5/4/2015	423103	4519501	7.6/0.4	17.8/19.5	36.8/37.4	7.93/8.32	437 (346/575)	13.5 (0/22.6)
17	5/4/2015	423127	4519505	8.6/0.4	17.7/20.7	36.7/37.2	8.22/8.32	389 (358/415)	9.1 (4.5/13.3)
18	5/5/2015	423052	4519471	14.4/0.8	16.3/19.6	36.8/37.6	7.82/8.25	757 (362/5490)	20.8 (0/275.3)
19	5/4/2015	423030	4519473	11.3/0.5	17.2/21.3	36.6/37.5	7.95/8.32	479 (362/781)	13.6 (3/19.7)
20	5/4/2015	423065	4519465	9.6/0.7	17.2/19.2	36.9/37.5	8.11/8.33	412 (375/490)	13.5 (1.4/18.6)
21	5/4/2015	423079	4519477	8.2/0.5	17.5/19.5	36.9/37.3	8.04/8.33	405 (359/463)	11.5 (0/16.1)
22	5/4/2015	423105	4519472	5.2/0.6	17.7/19.4	36.9/37.0	8.30/8.32	350 (344/363)	9.7 (7.6/10.5)
24	5/4/2015	423102	4519492	9.8/0.2	17.5/22.1	36.4/37.4	7.89/8.32	483 (369/769)	14.1 (0/24.1)
25	5/4/2015	423034	4519444	6.1/0.5	17.9/21.1	36.8/37.2	8.29/8.32	355 (342/386)	10.3 (8.9/11.3)
26	5/4/2015	423072	4519424	10.4/0.4	17.1/20.1	36.7/37.5	8.18/8.33	374 (344/438)	9.5 (2.7/12.8)
27	5/4/2015	423145	4519470	11.5/0.4	17.4/21.2	36.7/37.4	8.23/8.33	367 (351/383)	9.6 (2.8/13.2)
28	5/4/2015	423110	4519447	12.1/0.6	16.4/19.3	36.9/37.7	8.07/8.32	465 (350/539)	10.8 (0.7/20.7)
29	5/4/2015	423111	4519454	11.9/0.4	17.4/20.8	36.7/37.4	8.17/8.32	403 (359/489)	11.6 (5.2/15.7)
31	5/4/2015	423037	4519403	10.4/0.4	17.1/20.1	36.7/37.5	8.18/8.33	374 (344/438)	9.5 (2.7/12.8)
32	5/5/2015	423093	4519470	13.2/3.7	16.9/18.4	37.0/37.5	7.58/8.26	731 (436/2093)	17.9 (0/50.3)
33	5/4/2015	423085	4519444	11.0/0.5	17.0/19.7	36.8/37.5	8.19/8.33	381 (348/426)	9.6 (2.5/14.6)
34	5/4/2015	423116	4519424	13.4/0.3	16.3/19.7	36.9/37.6	8.13/8.32	407 (353/447)	9.2 (0/15)
35	5/5/2015	423099	4519462	13.4/0.8	16.9/19.6	36.8/37.5	7.34/8.25	950 (362/5025)	20.6 (0/70.8)
36	5/4/2015	423138	4519418	13.1/0.5	16.9/20.4	36.9/37.5	8.22/8.32	362 (348/375)	8.6 (1.3/11.5)
37	5/4/2015	423092	4519508	7.3/0.5	17.9/21.3	36.7/37.3	8.16/8.32	402 (354/482)	12.9 (4.9/17.9)
38	5/4/2015	423103	4519455	9.9/0.1	17.6/21.8	36.5/37.3	8.19/8.33	384 (366/428)	12.5 (4.8/15.4)
39	5/4/2015	423113	4519367	15.8/0.3	15.5/19.6	36.8/37.8	8.11/8.33	404 (348/449)	9.5 (0/15.1)
40	5/4/2015	422990	4519545	12.5/0.6	17.4/20.1	36.7/37.5	8.01/8.32	450 (359/642)	12.9 (0/21.3)
41	5/4/2015	423002	4519509	12.8/0.4	17.3/21.1	36.7/37.5	8.04/8.32	423 (364/545)	10.7 (0/16.4)
42	5/4/2015	423002	4519494	12.4/0.2	17.4/21.5	36.8/37.4	8.10/8.32	418 (362/532)	11.9 (0.6/18.5)
43	5/4/2015	423004	4519471	13.1/0.3	17.0/21.2	36.5/37.5	8.16/8.32	394 (360/443)	9.6 (1.2/14.1)
44	5/5/2015	422958	4519591	12.0/0.6	17.0/19.9	36.9/37.5	8.10/8.26	415 (373/482)	4.3 (0/9.2)
45	5/5/2015	422955	4519539	12.7/0.4	16.6/21.7	36.7/37.6	8.04/8.26	426 (375/537)	3.9 (0/11.2)
46	5/5/2015	422956	4519490	13.3/0.6	16.2/20.7	36.9/37.6	8.06/8.26	426 (371/473)	4 (0/9.2)
47	5/5/2015	423002	4519600	12.4/0.4	16.6/20.5	36.8/37.6	8.07/8.25	426 (384/507)	3.5 (0/8.5)
48	5/5/2015	423003	4519651	10.1/0.4	17.0/22.5	36.6/37.5	8.15/8.26	404 (379/419)	3.7 (0/8.4)
49	5/5/2015	422956	4519643	11.4/0.5	16.9/21.8	36.8/37.5	8.14/8.26	410 (385/443)	3.5 (0/9.1)
50	5/5/2015	422895	4519595	11.8/0.4	16.7/22.4	36.5/37.6	8.13/8.26	408 (394/438)	3.2 (0/8.5)
51	5/5/2015	422907	4519551	12.3/0.5	16.3/21.8	36.2/37.6	8.11/8.26	410 (386/439)	3.3 (0/8.1)
52	3/10/2014	423076	4519446	12.0/1.2	19.0/19.1	36.9/36.9	7.92/8.32	615 (464/3581)	24.7 (7.4/133.2)
1B	5/5/2015	422698	4518483	20.3/0.1	15.2/20.0	36.8/37.7	8.18/8.25	370 (359/387)	0
2B	5/5/2015	422656	4518495	20.4/0.5	14.9/20.1	37.0/37.8	8.18/8.27	378 (364/406)	2.6 (0/6)

[a]For each of the 49 sites, minimum (min) and maximum (max) values are reported. The depth range of each profiles is given in meters below sea level (b.s.l.). Temperature is in °C, salinity in ‰, pH, and CO_2 partial pressure (pCO_2) in μatm (the mean value is also listed). Total dissolved excess carbon (C_{ex}) is expressed in g/m^3, and calculated in reference to background site 1B.

via a 50 m-long transmitting cable connected to the instrument. During the measurements, we routinely operated cycles of CO_2-sensor zeroing (each lasting 120s) and flushing (each lasting 480 s), with these measurements used during postprocessing to correct for instrumental drift [see *Fietzek et al*., 2014 for details]. Following the procedure illustrated by *Fiedler et al*. [2013], we calculated that there was a trivial zero drift during the measurement period, with the zero signal deviating by only ~0.3–3% from the mean value. The sensor response time (expressed as T_{63}) was 20 ± 2 s (mean ± maximum deviation) at the surface and 30 s at a depth of ~20 m. This response time remained constant on 4 and 5 May and was used to correct the collected data using the time-lag correction algorithm of *Miloshevich et al*. [2004].

Vertical seawater profiles of the pressure, salinity, temperature, and pH were determined using the Ocean Seven 303 CTD multiparameter probe (IDRONAUT). Our specific probe was equipped with (i) a high-

Table 2. Chemical Composition of Local Seawater (SW) and SdF Seafloor Thermal Vents[a]

Sample	Data	East	North	T (°C)	pH	HCO_3 (ppm)	Cl (ppm)	SO_4 (ppm)	Na (ppm)	K (ppm)	Mg (ppm)	Ca (ppm)	$\delta^{18}O$ (‰)	δD (‰)	CO_2 (g/L)	TDIC (g/L)
Local SW	8/1/2000			20	8.10	161	22390	2906	12250	446	1397	447	1.50	10.00	n.d.	0.12
SdF submarine thermal waters																
CFS4a	8/1/2000	423058	4519484	82	6.40	285	18280	1682	11170	445	861	531	1.51	0	n.d.	n.d.
CFS4b	1/5/2005	423058	4519484	82	6.08	272	19060	1844	10750	439	968	610	1.51	1.53	425	0.63
CFS4c	1/5/2005	423058	4519484	82	6.01	281	18650	1854	10590	438	966	625	1.54	6.00	559	0.77
CFS4_H0.5	6/27/2006	423076	4519447	60	n.d.	n.d.	13980	845	7815	340	462	301	1.55	2.46	n.d.	n.d.
CFS4_H1.5	6/27/2006	423076	4519447	103	5.95	448	11120	588	5941	270	202	299	1.65	−11.3	638	0.97
Terme di Nerone thermal water wells (NTW)																
NTW_1	5/14/2013	422123	4519918	75	6.79	355	10080	299	6330	196	25.7	253	−1.63	−14.2	111	n.d.
NTW_2	5/14/2013	422123	4519918	76.5	7.16	360	11400	407	7420	262	73.5	276	−1.30	−12.2	126	n.d.

[a]The composition of two thermal waters in the CF onshore are shown for comparison. Total dissolved inorganic carbon (TDIC) is the sum of dissolved CO_2 and alkalinity value.

precision (0.05% of full scale) pressure transducer working in the range of 0–1000 dbar (10^4-10^8 Pa); (ii) a temperature sensor working in the range of 1–50°C, with a resolution of 0.001°C and accuracy of 0.005°C; (iii) a pH electrode with a resolution of 0.01 pH units and an accuracy of 0.001 pH units, and (iv) a seawater conductivity sensor working in the range of 0–70 mS/cm, with a resolution of 0.001 mS/cm and an accuracy of 0.007 mS/cm. The CTD data, acquired at 1Hz, were stored in the internal memory and also transferred (at 8 Hz with 16 bit solution) in real time to a PC via a special transmitting cable. The pressure in decibar (dbar) was converted into depth in meters b.s.l. using the UNESCO seawater algorithms [*Fofonoff and Millard*, 1983], and conductivity data were used to derive seawater salinities.

Our seawater vertical profiles (crosses in Figure 1a) were acquired along a (quasiregular) measurement grid generally with a spacing of 50 m, but with the spacing reduced to 25 m in the SdF area above the hydrothermal vents. In total, 47 geochemical vertical profiles (Table 1) were obtained in an area of $\sim$ 0.14 km^2. Additionally, two vertical profiles were obtained at the exit of Pozzuoli Bay (sited 1B and 2B in Figure 1), and are taken to be representative of the local seawater background. At each site, the CO_2 sensor and the CTD probe were simultaneously lowered from a small boat down to the seafloor, and then raised up to the seawater surface at a descent/ascent rate of $\sim$5 cm/s. While performing the measurements along each vertical profile, and at each $\sim$5 cm step, the CO_2 sensor/CTD assemblage was stopped (and maintained at a constant depth) for a few seconds, in order to allow the sensors to fully equilibrate. Given the irregular seafloor morphology of the SdF area, the vertical profiling at four sites (n. 18, 32, 35, and 52; see Table 1 and red crosses in Figure 1a) was assisted by a scuba diver so as to ensure that the sensors reached (and measured) the near-vent plumes of four distinct major degassing vents.

3.1.3. Current Measurements

On 4 and 5 May 2015, concurrently with the above geochemical measurements, we determined the trajectories and velocities of the water current using the drifter prototype described in *Nasello and Armenio* [2016]. In our specific application, the drifter trajectory was remotely sampled every minute using an integrated GPS system, and transmitted via radio to the operator. The GPS positions were corrected by means of the Wide Area Augmentation System (WAAS), yielding overall positioning errors of $<$2 m. During these measurements, the drifter was released at different points around the SdF area, and left free to float for 1 h. The acquired position data (N and E coordinates) were postprocessed to derive the current trajectories and velocities in the investigated area. The error of the derived velocities was $<$1 cm/s.

3.1.4. Direct Sampling and Analysis of Fluids

The SdF submarine fluid emissions (green open squares in Figure 1a) were directly sampled in three campaigns performed in 2000, 2005, and 2006 (Table 2). The sampling concentrated on a main emission vent that formed a clearly visible ascending plume of hot water (supporting information Movie S2). This vent (CFS4 in Table 2) was sampled once in 2000 (CFS4a in Table 2) and twice in 2005 (CFS4b and CFS4c in Table 2). In 2006, hot-water samples were taken from small holes drilled in the seafloor soft sediments that were from 0.5 m deep (at 60°C; CFS4H0.5 in Table 2) to 1.5 m (at 103°C; CFS4H1.5 in Table 2). For comparison, we also discuss data for two onshore Terme di Nerone thermal wells (*NTW* in Figure 1) (NTW_1 and NTW_2 in Table 2). Chemical and isotopic analyses were performed at the INGV-OV laboratories following the methods described by *Caliro et al.* [1998] (Table 2).

3.2. C Speciation in Seawater

The marine CO_2 system [*Millero*, 1995] was fully characterized by combining the data measured by the CTD and HydroC sensors. For each measurement site and depth, we calculated the total dissolved C (C_{TOT}) contents and dissolved C speciation (supporting information Table S1) using the coacquired pH and pCO_2 readings (Table 1). We calculated C_{TOT} as the sum of dissolved H_2CO_3 (below referred as $CO_{2(aq)}$), HCO_3^- and CO_3^{2-}, derived from measured pH and pCO_2 values, by solving the following equations:

$$K_0 = K_{CO_2} = \frac{aH_2CO_3}{pCO_2 \cdot aH_2O} \quad (1)$$

$$K_1 = K_{HCO_3^-} = \frac{aHCO_3^- \cdot aH^+}{aH_2CO_3} \quad (2)$$

$$K_2 = K_{CO_3^{2-}} = \frac{aCO_3^{2-} \cdot aH^+}{aHCO_3^-} \quad (3)$$

where K_0 is the CO_2 Henry's law constant, K_1 (= $KHCO_3^-$) and K_2 (= KCO_3^{2-}) are the first and the second dissociation constants of acidic C, respectively, *a* stands for activities, and pCO_2 is the CO_2 partial pressure in equilibrium with the solution. We used the empirical equations of *Weiss* [1974] and *Millero* [1995] to derive K_0, K_1, and K_2 as functions of salinity (*S*, in per mille) and temperature (*T*, in kelvin).

4. Results

4.1. Geophysical Data

Figures 2 and 3 show a seismostratigraphic reconstruction and a morphobathymetric model of the SdF area, respectively.

Three seismic cross sections, all intersecting the SdF area, are illustrated in Figures 2b–2d. The imaged seismic horizons correspond to a geological sequence that is ~70 m thick (depths were calculated for the two-way travel-times using a P-wave velocity of 1600 m/s). The analysis of seismic sequences reveals five distinct seismostratigraphic units (supporting information Table S2). These units are distinguished based on their specific attributes, including amplitude, lateral continuity, frequency, external shape, and internal geometry. The seismic characteristics of the analyzed sequences are summarized in the synoptic chart of supporting information Table S2, and their geometry is well illustrated by the characteristic section shown in Figure 4 (see Figure 1 for its location). The following units are identified:

1. *Unit a* appears as a flat-lying plan-parallel aggradational sequence in the EV and BV areas (Figure 1), progradational in the seaward edge of terraces, and chaotic to divergent in the shallow areas (supporting information Table S2). In the deepest part of the bay, *Unit a* is involved in folds with a wavelength of 2 km (Figure 4). This unit is interpreted as the sedimentary cover of a transparent-to-chaotic unit, representing the acoustic basement.

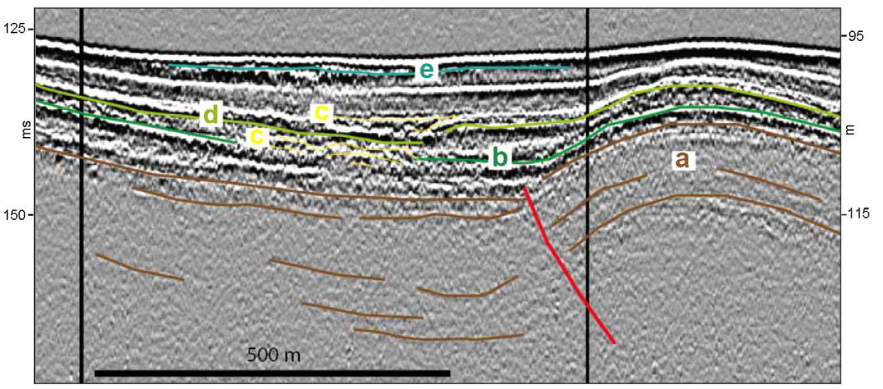

Figure 4. Seismostratigraphic cross section (see Figure 1 for location) identifying the seismic basement and five seismic horizons (a–e) discussed in the text and supporting information Table S2 (see section 4.1).

2. *Units b,-d, and -e* (supporting information Table S2) are imaged as bright reflectors with high amplitudes, and are located at depths of 1–8 m (Figures 2b–2d and 4). The deepest unit is continuous throughout the area, while the two shallower ones are often discontinuous.
3. *Unit c* (supporting information Table S2) exhibits a geometry ranging from chaotic to wavy-hummocky, and is often organized in lens-shaped bodies, as is typical of mass-gravity deposits (Figures 2d and 4). It is located both immediately below and above the tephra layer of *Unit d* (Figure 4).

Combined seismostratigraphic and morphobathymetric analyses constrain the morphostructural setting of the SdF area. Our data reveal an uneven seafloor, with several NNW-SSE and NE-SW-trending morphostructural features (Figures 2 and 3). Two main structures are identified: the SdF ridge and a depression to the W of it.

Our results demonstrate that the SdF consists of a NNW-SSE-trending elongated ridge (see Figures 2a and 3a), lying on a terraced area at ∼10 m b.s.l. The Roman "pilae" (inset of Figure 3a1) were funded over this natural ridge. The ridge is bordered by faults trending from NNW-SSE to N-S (red faults in Figure 2a), downthrowing well-defined wavy seismic horizons (red faults Figures 2b–2d). The displacement of these horizons points to contractional kinematics (Figure 2b). Toward the S, the SdF ridge is bounded by a near-vertical NE-SW-oriented extensional fault system (*EFS* in Figure 2) that has a maximum displacement of ∼5 m (Figure 3b). This structure interrupts the gentle slope (∼0.2°) of the inner shelf, and is followed seaward by a flat terraced area (for about 38 m) bounded by a morphological break, which is interpreted as the inner-to-outer shelf transition (Figures 1 and 2a). Seismostratigraphic data show a progradational pattern (*p* in Figure 2c), which we interpret as being formed while the sea level was in a steady state.

W of the SdF ridge, morphobathymetric and seismostratigraphic data provide evidence of the existence of a ∼300 m-wide depression that developed in the N-S direction (Figures 2 and 3). In the proximal sector (Figures 3b and 3c), the depression takes the form of a large U-shaped channelized area (perpendicular to the coastline), with 0.3° dipping slopes that are interrupted on both the eastern and western flanks by 3–4° dipping scarps. The flanks are 7 m (W) and 6 m (E) high, whilst the thalweg is located at a depth of 12.3 m b.s.l. (Figure 3b). Toward SE, in a NE-SW profile (Figure 3c), the channel becomes V-shaped and asymmetrical, with a sharper NE flank. The depression is bordered by two Roman buildings, located at the top of the two scarps: Villa dei Pisoni to the SW (*VP* in Figures 1 and 3), and SdF to the NE. Seismic profiles (e.g., Figure 2d) reveal that the depression is controlled by faults, being bounded by a system of two nearly parallel (N-S-trending) extensional faults displaced by 6 m. We interpret this depression as a graben. Toward the SE (Figure 3a), an additional, wider depression develops in the NW-SE direction (Figure 3d) that is 200 m wide, 400 m long, and 30 m deep (its top and bottom are at 15 and 45 m b.s.l., respectively). This depression contains some elements of the SdF pilae complex (see inset in Figure 3a2), and is therefore more recent than the Roman-period.

4.2. Seawater Vertical Profiles

The seawater column was investigated to a maximum depth of 15.8 m b.s.l in the SdF area (Figure 1a and Table 1). Greater depths (up to 20.4 m b.s.l) were explored only at background sites 1B and 2B (Figure 1 and Table 1).

Figure 5 shows vertical profiles of temperature, salinity, pH, and pCO_2 along the seawater column. The background vertical profiles (sites 1B and 2B; Table 1) are also shown for comparison.

The seawater temperature in the SdF area ranges from 15.5°C to 22.4°C (Figure 5a). The temperature spread is largest near to the surface, such as from 18.5°C to 22.4°C at depths of $<$1.5 m b.s.l. In contrast, a uniform temperature versus depth trend is observed deeper in the water column. The seawater temperature decreases with depth at all sites (including along the background vertical profiles at an average rate of ∼0.2°C/m, from ∼19°C (at a depth of 1.5 m b.s.l.) to ∼15°C (at a depth of 20 m b.s.l.). Similarly, the seawater salinity in the SdF area (Figure 5b) shows a larger heterogeneity (from 36.2‰ to 37.5‰) at depths of $<$1.5 m, and then increases monotonically with depth along the seawater column, from a mean value of 37‰ at the surface to ∼38‰ at the seafloor. The more-distal (background) sites (1B and 2B in Figure 1 and Table 1) exhibit the most regular salinity versus depth patterns.pH and pCO_2 exhibit complex variations along the SdF seawater column (Figures 5c and 5d). In the SdF area, pH is consistently lower (range: 7.34–8.33) and pCO_2 is consistently higher (range: 337–5490 μatm, equal to 34–556 Pa) than the values measured in the background vertical profiles (sites 1B and 2B in Figure 5c: pH ∼8.23 and pCO_2 ∼370 μatm, equal to

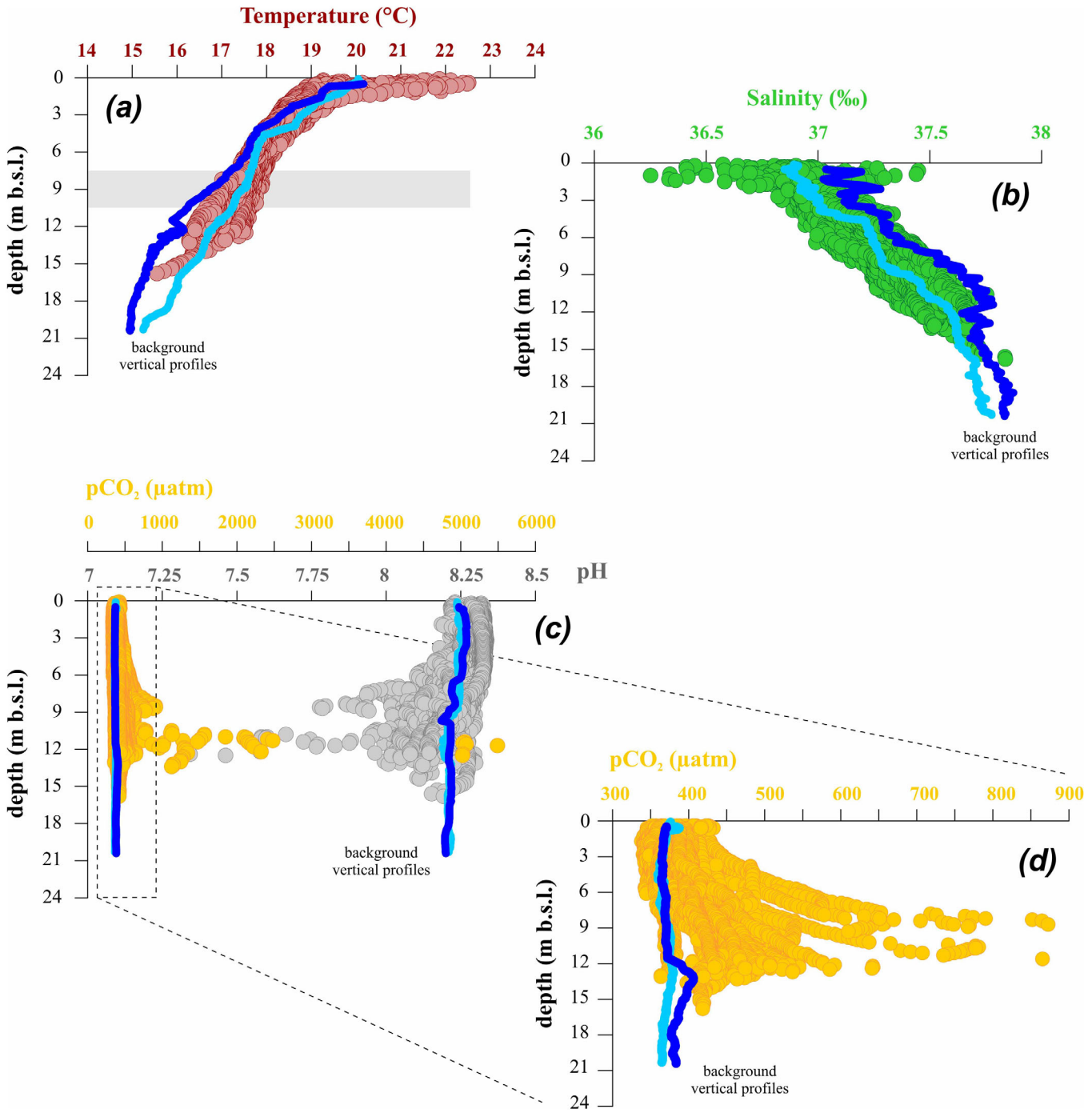

Figure 5. Vertical trends of (a) temperature, (b) salinity, (c) pCO_2 and pH along the seawater column (SdF area). (d) Detail of the pCO_2 profiles. All plots include the background vertical profiles 1B and 2B (see Figure 1 and Table 1) represented by light and deep-blue curves, respectively, for comparison. The gray-shaded area in Figure 5a identifies the 3 m thick layer, centered at depth of 9 m b.s.l., that was used to investigate the correlation between temperature and C_{ex} (see Figure 12).

37 Pa). The pH and pCO_2 values exhibit opposite vertical trends: the former decreases while the latter increases along the seawater column (Figure 5c). These concomitant variations are particularly well resolved at depths of 8–13 m b.s.l., where pH decreases to 7.30 as pCO_2 peaks at ~5500 µatm (557 Pa) (Figure 5c). Such large and correlated variations in pH and pCO_2 support the existence of point sources on the seafloor that acidify seawater and are rich in CO_2.

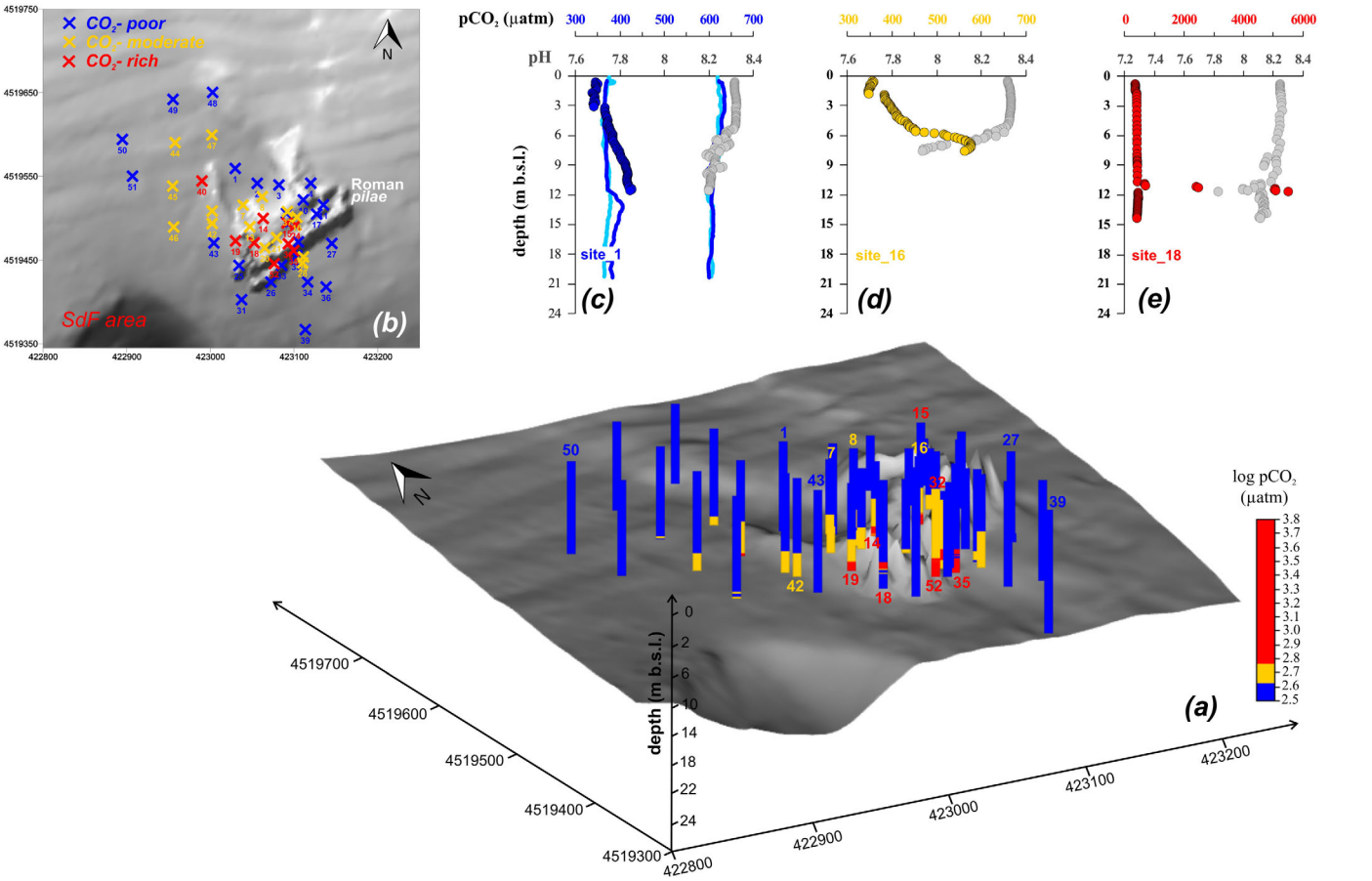

Figure 6. (a) Vertical profiles of log pCO_2 in the seawater column at the SdF measurement sites (their locations are shown in the map in (b)). (b) Measurement sites ranked into three main groups (see colored crosses) depending on the pCO_2 peak registered along the seawater column. Examples of vertical profiles of pCO_2 and pH trend are illustrated for each group: (c) a *CO_2-poor* site, (d) a *CO_2-moderate* site, and (e) a *CO_2-rich* site. Figure 6c includes the vertical profiles obtained at the background sites 1B and 2B (see Table 1) for comparison (as light and deep-blue curves, respectively).

With the aim of identifying the sectors of the SdF area characterized by anomalous seawater contents of dissolved CO_2 (higher than the background levels), we categorize the SdF sites into the following three distinct subgroups (see crosses in Figure 6b) based on the peak pCO_2 values measured along each of the measured seawater vertical profiles (see Table 1):

1. *CO_2-poor*, with $pCO_2 < 450$ μatm (46 Pa) or log $pCO_2 < 2.65$ (see blue crosses in Figure 6b);
2. *CO_2-moderate*, with $pCO_2 > 450$ μatm (46 Pa) but < 600 μatm (61 Pa); (yellow crosses in Figure 6b);
3. *CO_2-rich*, with $pCO_2 > 600$ μatm (61 Pa), or log $pCO_2 > 2.8$ (red crosses in Figure 6b).

This categorization is based on the mean (445 μatm, approximated at 450 μatm) and standard deviation ($\sigma = 152$ μatm, approximated at 150 μatm) of our pCO_2 data, leading to a mean plus-one-standard-deviation (1σ) anomaly threshold of ~600 μatm.

The *CO_2-poor*, *CO_2-moderate*, and *CO_2-rich* categories exhibit somewhat distinct pH versus depth and pCO_2 versus depth relationships (Figures 6c–6e). At the *CO_2-poor* sites (e.g., Figure 6c), the pH values are often higher than the background (>8.25) and frequently associated with $pCO_2 < 370$ μatm (37 Pa). Such high pH values (and low pCO_2 values) are not uncommon in highly productive coastal zones during early summer [*Hansen*, 2002; *Middelboe and Hansen*, 2007], when biological photosynthesis scavenges C delivered by the atmosphere, benthic respiration, and calcification [*Frankignoulle and Bouquegneau*, 1990; *Semesi et al*., 2009; *Kerrison et al*., 2011]. The *CO_2-poor* sites (e.g., site 1 in Figure 6c) often show an initial pH increase with depth followed by an inversion, suggesting that biological activity is concentrated in the upper few meters. In contrast, the opposite pH and pCO_2 vertical trends are more marked and regular in the *CO_2-moderate* (e.g., Figure 6d) and *CO_2-rich* (e.g., Figure 6e) groups. Moderate (8.30–8.00) to low (<8.00) pH values are

systematically associated with pCO_2 values of 400–600 μatm (41–61 Pa) and >600 μatm (61 Pa), respectively (Figures 5c and 6d and 6e).

Figure 6a illustrates the three-dimensional (3-D) distribution of pCO_2 values in the SdF area. Figures 6a and 6b demonstrate that the lowest pCO_2 values (<450 μatm, equal to 46 Pa; or log $pCO_2 < 2.65$) are consistently detected at the periphery of the investigated area (e.g., *CO_2-poor* sites 1, 27, 39, 43, and 50; blue crosses in Figure 6b). The *CO_2-moderate* sites (yellow crosses in Figure 6b) all typically exist at the margins of the Roman pilae (e.g., sites 7, 8, 16, and 42 in Figures 5a and 5b), where peak CO_2 values up to ~600 μatm (61 Pa or log pCO_2 ~2.80) are detected, in the deepest parts of the profiles. Finally, the anomalous *CO_2-rich* sites (e.g., sites 14, 15, 18, 19, 32, 35, and 52; red crosses in Figure 6b) are all systematically observed in the central sector of the SdF area, where peak pCO_2 values (>600 μatm, equal to 61 Pa; and up to ~5500 μatm, equal to 557 Pa) are detected at depths of 12–14 m b.s.l. (see also Figure 5c), close to the seafloor and within the Roman pilae (Figures 6a and 6b).

Figures 7b and 7c illustrate that C_{TOT} is typically higher at *CO_2-moderate* and *CO_2-rich* sites (section 3.2 and supporting information Table S1) than the background (site 1B; Figure 7a and supporting information Table S1). For example, at *CO_2-rich* site 18 (Figure 7c), C_{TOT} peaks at ~25 mmol·kg^{-1} in the deepest part of the vertical profile (~11–12 m b.s.l.), which is an order of magnitude higher than the peak C_{TOT} in the background (~3 mmol·kg^{-1}; Figure 7a).

The results of speciation calculations (see section 3.2) are shown in Figures 7d–7f. The HCO_3^- is the most abundant species (82–95% of C_{TOT}) at all sites, followed by CO_3^{2-} (2–18% of C_{TOT}) (Figures 7d–7f). $CO_{2(aq)}$ constitutes only a small fraction of C_{TOT} (0.3–3.5%), but its (relative) abundance increases—at the expenses of CO_3^{2-}—from the background (Figure 7d) to the *CO_2-moderate* (Figure 7e) and *CO_2-rich* (Figure 7f) sites.

4.3. Hydrodynamic Measurements

The GPS positions registered by the drifter were used to derive the trajectories and velocities of the surface current in the SdF area. The results are illustrated in Figures 11a and 11b. On both measurement days (4 and 5 May 2015), the float-drifter movements demonstrate a NNW-trending local surface seawater current, with mean speeds of 9 and 14 cm/s, respectively (see dots in Figure 11a and crosses in Figure 11b). The vertical distribution of the current speed/trajectory was not measured, although it was qualitatively assessed at ~10 cm/s by the scuba divers. From a hydrodynamic point of view, seawater can be approximated as a turbulent viscous fluid that flows near a solid boundary with a no-slip condition (i.e., zero velocity of the fluid at the fluid-solid boundary). In this assumption, a logarithmic velocity profile can be predicted along the water column, from zero at the seafloor to a maximum at the air-seawater boundary [*Anwar*, 1996; *Marusic et al.*, 2010; *De Serio and Mossa*, 2014]. Assuming a well-mixed turbulent water column with no stratification, the surface current velocities (of 9 and 14 cm/s on the two measurement days; Figures 11a and 11b) can therefore be used to estimate current velocity (u_z) at any depth (z) along a seawater vertical profile:

$$u_z = \frac{u_*}{k} \ln\left(\frac{z}{z_0}\right) \tag{4}$$

where u_z is the mean flow velocity at depth z, k is the von Karman constant (typically 0.4), and u_* *and* z_0 *are computed assuming zero velocity at the seafloor, and maximum velocity at the surface (as measured by the drifter). Using this approach, we calculated trivial variations in the current velocity along the ~12 m seawater column, with average velocities of 8 and 12 cm/s on the two measurement days.*

Based on our results above, we assume in our CO_2 flux calculations below (section 5.2) that the time-averaged current velocity on 4 and 5 May was 10 ± 2 cm/s.

4.4. Vent-Fluid Chemistry

The chemical composition of the SdF submarine thermal waters (Table 2 and Figure 1a) is compared in Figure 8 with local seawater (local SW in Table 2) and with the onshore NTW (Figure 1 and Table 2), which are located only a few kilometers N of the SdF area.

All SdF thermal waters have an Na-Cl composition (Table 2) in which the content of total dissolved solids (18–33 g/L) is lower than that in the local seawater (40 g/L). This suggests that the thermal water chemistry is controlled by mixing between pure thermal water (of relatively low salinity) and seawater.

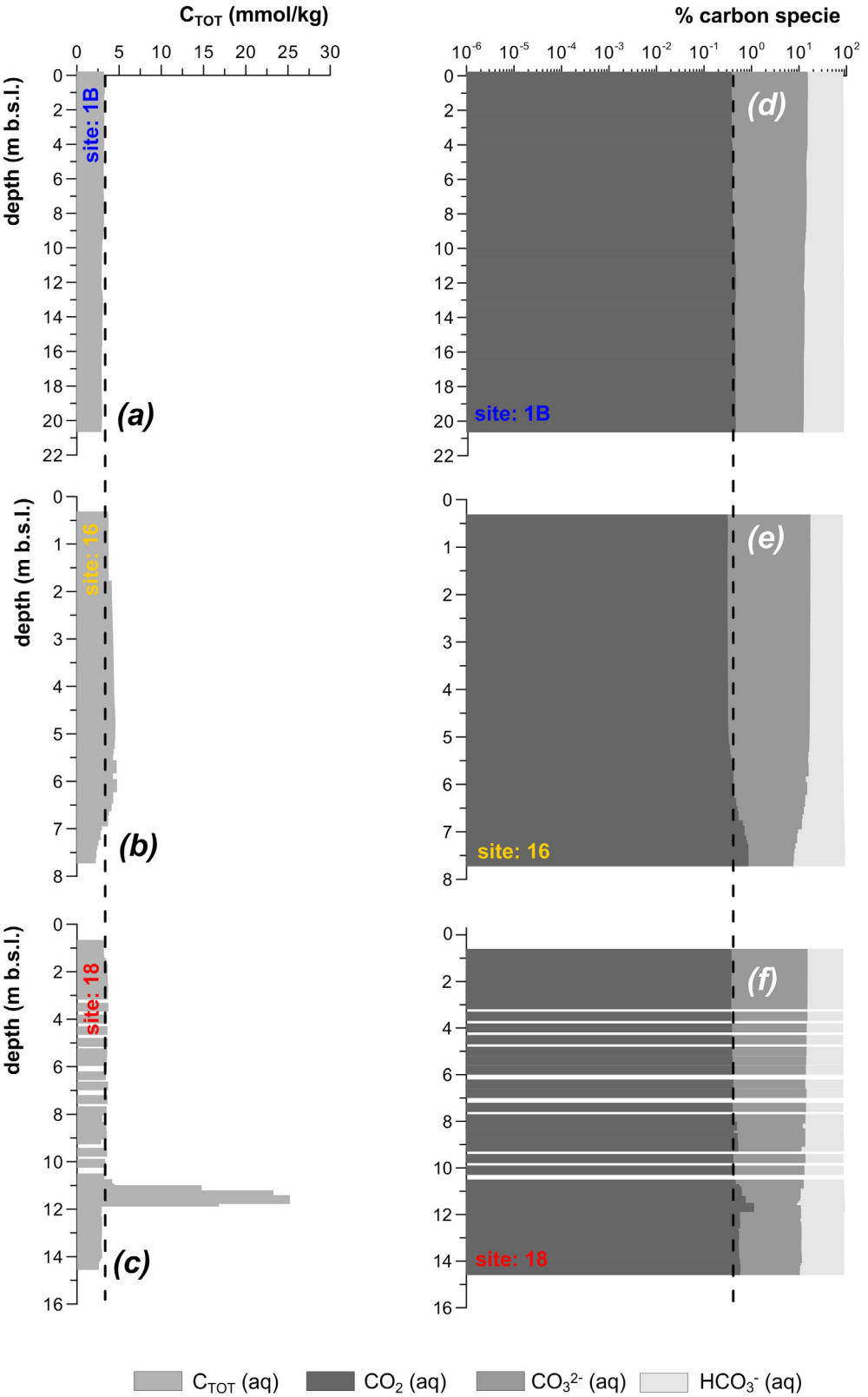

Figure 7. Vertical profiles along the seawater column of (a–c) C_{TOT} and (d–f) C speciation (expressed as $\%CO_{2(aq)}$, $\%HCO_3^-$, and $\%CO_3^{2-}$). Examples are shown for *CO_2-poor* (a and d), *CO_2-moderate* (b and e) and *CO_2-rich* (c and f) sites (see also the map in Figure 6b). The dashed vertical lines identify the anomaly thresholds for C_{TOT} (a–c) and $\%CO_2(aq)$ (d–f), which were fixed as the peak values registered at the background site (a–d).

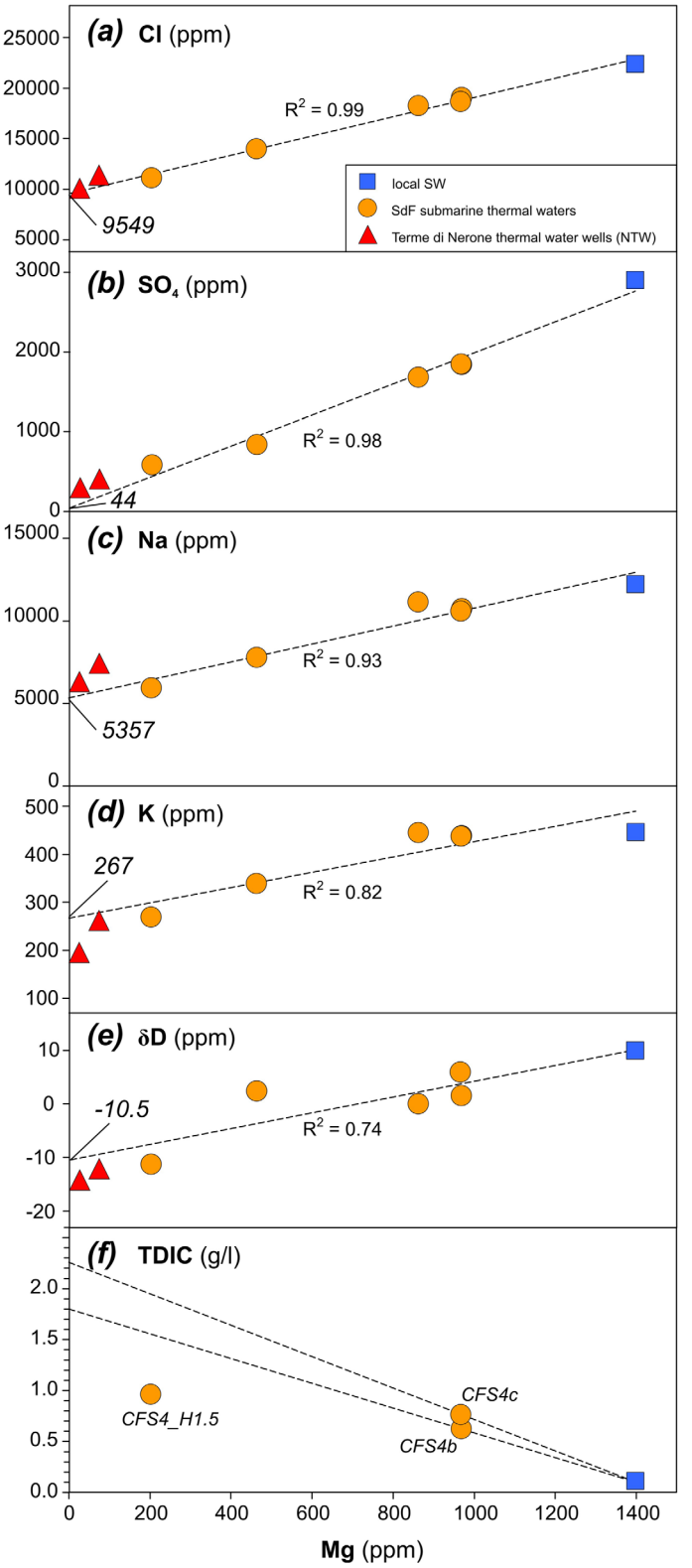

Figure 8. Binary plots illustrating the chemistry of the SdF submarine thermal waters. In each plot, Mg (*x* axis) is used as tracer of mixing between seawater and thermal end-member, and is plotted against (a) Chlorine, (b) SO_4, (c) Na, (d) K, (e) isotopic composition (as δD), and (f) C_{TOT} expressed as dissolved CO_2 in g/L). Dashed lines describe mixing between seawater and a supposed thermal end-member, having Mg = 0.

Figure 8 shows the mixing relationships using Mg as a tracer. The Mg content is very high in seawater and, in principle, very low in thermal waters. The Mg content of thermal waters strongly depends on temperature, due to it being controlled by temperature-dependent reactions between hydrothermal solutions and secondary minerals, such as chlorites (clinochlore) or other Mg-bearing minerals (e.g., montmorillonites and saponites) [*Ellis*, 1971; *Giggenbach*, 1988]. Owing to these reactions, Mg concentrations in pure geothermal solutions are typically on the order of 1 ppm or less, and are therefore negligible compared to seawater (i.e., Mg = 1400 ppm in the local seawater).

We here assume that the thermal SdF end-member has Mg = 0, for which we estimate the original contents of Cl (9549 ppm), SO_4 (44 ppm), Na (5357 ppm), and K (267 ppm) for the pure thermal component by linear fitting of the mixing trends in Figures 8a–8d. The same calculation for deuterium indicates that the original thermal end-member is isotopically lighter (δD versus SMOW = $-10.5‰$) than local seawater (δD versus SMOW = $+10‰$) (Figure 8e). The measured compositions of NTW strongly support the reliability of such estimations, with the NTW samples plotting close to the estimated pure thermal component in each plot in Figures 8a–8e.

We used the above-derived Na and K concentrations in the pure thermal component to estimate the equilibrium temperature of the fluids at depth. We used the relation of

Giggenbach [1988] to evaluate that the equilibration temperature was 179°C. Similar temperatures were measured in the shallowest parts (at depths up to a few hundreds of meters) of the Mofete geothermal wells (*MGW* in Figure 1) that were drilled by the Italian company AGIP at the beginning of the 1980s [*De Vivo et al*., 1989] in the north-western margin of CFc.

Total dissolved inorganic C (TDIC; Table 2) was only determined in three samples (CFS4b, CFS4c, and CFS4_H1.5 in Table 2), in which free CO_2 was determined by extracting the dissolved gas using the method described in *Caliro et al*. [2005], and then summed to measured alkalinity to obtain TDIC values. The so-derived TDIC ranges between 0.63 and 0.97 g/L, which is five to 10-fold higher than the value in seawater (0.12 g/L) (Figure 8f). Using the assumption of 0 Mg, and by considering the mixing of the CFS4c sample with seawater, we estimate a TDIC of $\sim$ 2.20 g/L for the pure thermal end-member (Figure 8f). We caution that this probably underestimates the real original CO_2 content of the thermal end-member due to significant (but unquantifiable) CO_2 loss from the thermal solutions occurring prior to discharge and sampling at the seafloor. The occurrence of CO_2 degassing prior to sampling is supported by the diffuse presence of CO_2-rich gas bubbles around the emission vents (see supporting information Movie S1), which is particularly evident in sample CFS4_H1.5 (Figure 8f).

5. Discussion

The data acquisition and analyses performed in this study have contributed to a better understanding of the largest submarine hydrothermal offshore manifestation of CFc volcano. We first derived age constraints on the studied sequences by calibrating our seismic profiles with independent chronostratigraphic data [*Sacchi et al*., 2014] (section 5.1). We then combined our geophysical data with independent onshore geological/volcanological information to derive structural constraints for the SdF ridge structure (Figures 1 and 2). Finally, our geochemical measurements, both along the seawater vertical profiles (Figure 5c) and at the seafloor vents (Figure 8), were used to evaluate the CO_2 and energy (heat) budget for the SdF hydrothermal system. We have defined a novel CO_2 flux quantification procedure that can be applied at any submarine hydrothermal manifestation worldwide.

5.1. Age Constraints

High-resolution seismostratigraphic data identified a late Quaternary succession that penetrated to a maximum depth of $\sim$70 m and consisted of several $\sim$10 m thick individual layers (Figures 2b–2d). We identified some distinct seismic units having specific attributes (characteristics and geometry; supporting information Table S2). These key seismic horizons were age-calibrated using the chronostratigraphic record of gravity cores reported for the same area by *Sacchi et al*. [2014].

Unit a (supporting information Table S2 and Figures 2 and 4) corresponds to the sedimentary cover of a transparent-to-chaotic unit, representing the acoustic basement. Correlating the obtained data with sparker seismic reflection profiles [*Sacchi et al*., 2014] led to the basement being interpreted as the NYT. As a consequence, *Unit a* can be dated as younger than 15 ka. Similarly, we infer from cross correlation that *Units b, d*, and *e* (supporting information Table S2) correspond to the three tephra layers described by *Sacchi et al*. [2014] based on core data as having inferred ages of 3.9 ka, AD 79, and AD 1538, respectively.

Linking the above seismic units with structural features (e.g., faults) constrains the age of the SdF relief. In the SdF area, seismic *Units a–d* are cut by both normal and reverse faults, while *Unit e* is typically missing (Figures 2b–2d). The most recent tectonic event is represented by N-S-trending reverse faults present in the SdF area and along the inner platform edge scarp (Figures 2b–2d). These faults dislocate the whole sedimentary succession up to *Unit d*, which is interpreted as the Pompeii eruption tephra [*Sacchi et al*., 2014]. From these results, we infer that the ridge-shaped SdF structure is younger than AD 79.

5.2. Structural Interpretation

In our seismic cross sections (Figure 2), the SdF area appears as a ridge, bordered by systems of both extensional and contractional N-S-trending faults. In view of our young age estimates, and the historical chronicles of *Guidoboni and Ciuccarelli* [2011] and *Giacomelli and Scandone* [2012], we suggest that the present-day SdF setting is structurally linked to the Monte Nuovo eruption in AD 1538 (Figure 1).

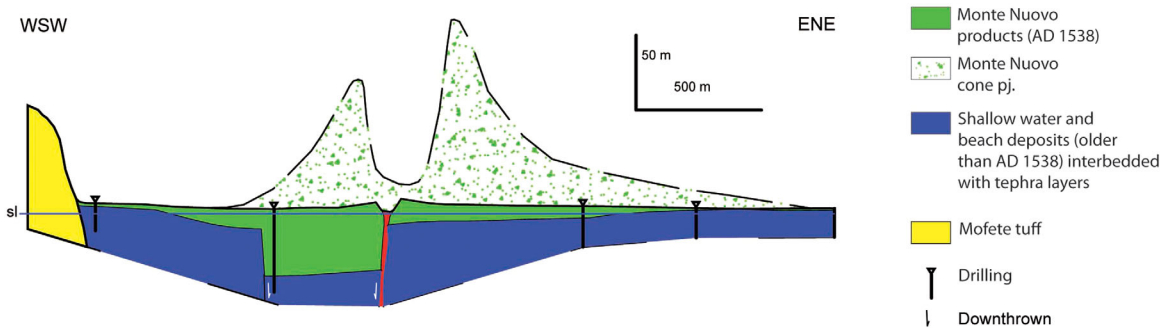

Figure 9. Geological cross section in the coastal area near to the Monte Nuovo eruption vent area (see Figure 1 for location). Geological units were identified based on surface geological features and shallow drillings. Red line shows the inferred position of the conduit of the southern Monte Nuovo vent.

We test this hypothesis by exploiting original geological data for the onshore sector of Monte Nuovo. We take into account both results of surface surveys [*Di Vito et al*., 2016] and subsurface data obtained from shallow (25–50 m) wells ("*Drilling*" in Figure 9). Combining these data makes it possible to reconstruct a simplified geological E-W cross section (Figure 9) along the coastline (see Figure 1 for the location). The profile crosses the southern slopes of the Monte Nuovo tuff cone; the morphologies of the cone and of the main crater appear as *Monte Nuovo cone pj* in the background of Figure 9.

Two feeding vents were active during the Monte Nuovo eruption [*Di Vito et al*., 2016]: (i) a principal vent, in the center of the cone, and (ii) a secondary vent to the S, which is near the coast and crossed by the profile of Figure 9 (also see Figure 1). The eruption lasted 1 week, and deposited a sequence of coarse-to-fine-ash pyroclastic flow deposits, and less abundant fallouts [*Di Vito et al*., 1987]. These pyroclastic units ("*Monte Nuovo products – AD 1538*" in Figure 9) exhibit large thickness variations, the most significant of which is a localized and abrupt thickening (up to 50 m) in a depression located W of the southern vent (Figure 9). The Monte Nuovo deposits are underlain by coastal-to-shallow-seawater sediments that formed between the Roman period and the 1538 eruption [*Di Vito et al*., 2016] ("*Shallow water and beach deposits* > *AD 1538*" in Figure 9). In correspondence with the depression, these deposits are encountered at depths (45–50 m b.s.l.) that are greater than those implied by their shallow deposition environment (∼0 m b.s.l.). We conclude that this depression was formed by a rapid (syneruptive) localized subsidence of the coastal sector. As the depression formed, probably controlled by syneruptive fault opening, the coastal deposits were eventually buried during the deposition of pyroclastic flows. A particularly interesting observations is that the reconstructed fault-bounded eastern limit of the depression (Figure 9) extends to the southern vent of Monte Nuovo [*Orsi et al*., 2009], where it is marked by a significant difference in height of the rim (see the Monte Nuovo profile in Figure 9). This suggests a ∼30 m down-throwing of the cone to the W, which is consistent with the subsurface data.

Localized subsidence is additionally evident in the present-day structure of the submerged Roman remnants of the Portus Iulius (harbor) area (*PI* in Figure 1) that is immediately to the S of Monte Nuovo [*Passaro et al*., 2103, and references therein]. Today the harbor remains partially preserved in its northeastern and southwestern sectors, where it consists of an alignment of large breakwater pillars (Figures 1 and 2a). In contrast, remnants of the harbor in the central sector (immediately in front of Monte Nuovo) are completely lacking or have been destroyed (Figure 10). While we thus believe that some subsidence occurred in this central sector, we argue that the present-day depth of Portus Iulius harbor (∼10 m b.s.l.) is shallower than the marine sediments encountered in our profile (45–50 m b.s.l.), which implies that the subsidence was largest along the coastal sector adjacent to Monte Nuovo (Figure 9).

The geological/structural information from Figure 9 was combined with morphobathymetric and seismostratigraphic data in this study in an attempt to link the onshore (Monte Nuovo) and offshore (SdF) sectors into a single interpretative deformation model. The sketch in Figure 10 proposes the existence of a single N-S-trending deformed area that extends from Monte Nuovo to the edge of the submarine platform. The presence of this N-S trending deformed area is supported by the following observations (listed from N to S):

1. Suspected down-thrown of the western part of the Monte Nuovo cone.
2. The subsidiary vent immediately S of the Monte Nuovo cone.

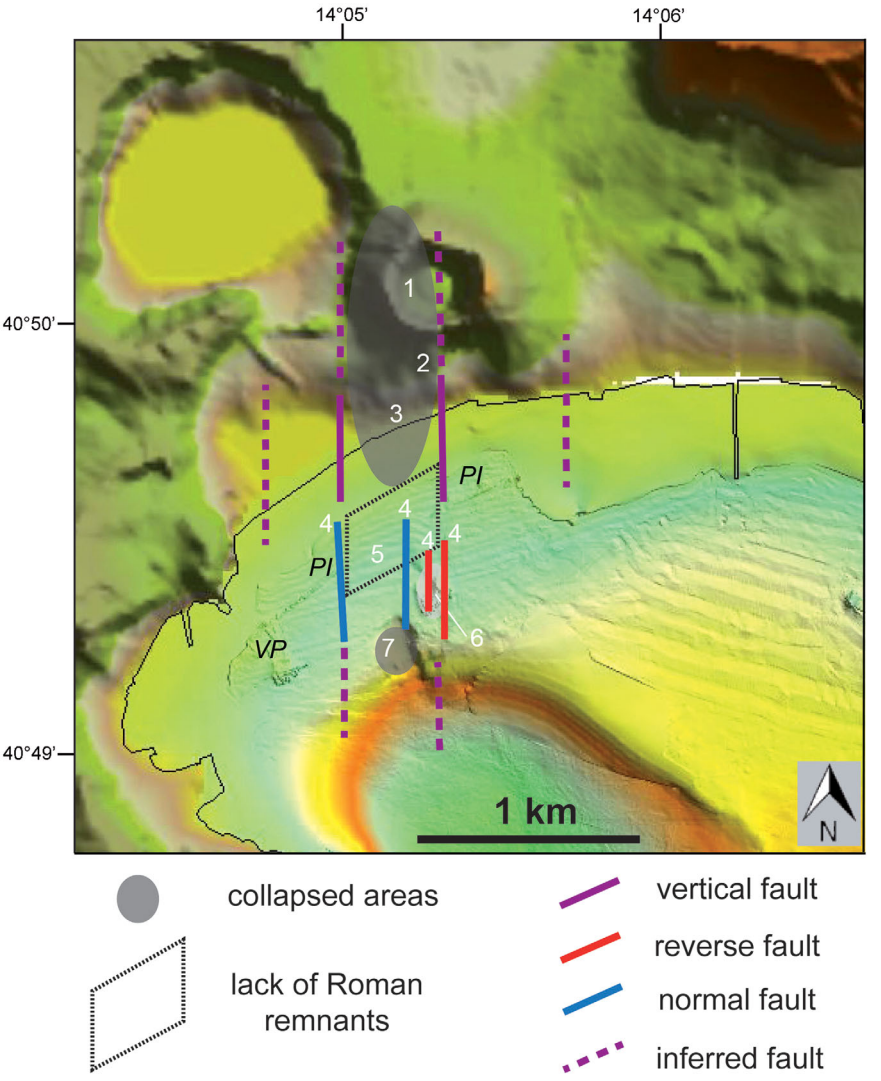

Figure 10. Combining the collected geological, drill-hole, morphobathymetric, seismostratigraphic, geochemical, and archaeological data to propose an interpretative structural model summarizing the possible deformation pattern associated with the Monte Nuovo eruption. Numbers 1–7 correspond to the geological-structural features that we used to identify the N-S-trending deformed area (see text for details). The NE-SW-trending faults shown in Figure 2 have not been reported here, since these are interpreted as not being related to the Monte Nuovo eruption deformation.

3. The buried depression along the coastline, evident in the cross section of Figure 9.
4. The offshore ~N-S trending normal and reverse faults.
5. The central sector of the Portus Iulius harbor; in this area, the absence of Roman remnants implies subsidence and burial underneath the Monte Nuovo deposits.
6. The actively degassing SdF ridge (Figures 6a and 6b).
7. The subcircular depression to the SW of the SdF area.

The deformed area stretching from the structures described in items 1–7 in this list is here interpreted as the surface expression of a N-S-trending fault system that, bounds a depression ("*collapsed areas*" in Figure 10). Structure 7, in particular, appears to be a localized subcircular depression associated with a mainly vertical collapse (Figure 10). It therefore exhibits the typical morphological features of pit-craters, which are small (diameter generally less than a few hundreds of meters) vertically collapsed structures that develop along rift zones. In such areas, pit-craters typically form in the apical parts of magma feeding dikes where, in correspondence with weaker host rocks, dike-opening leads to surface collapses [*Okubo and Martel*, 1998; *Roche et al.*, 2001].

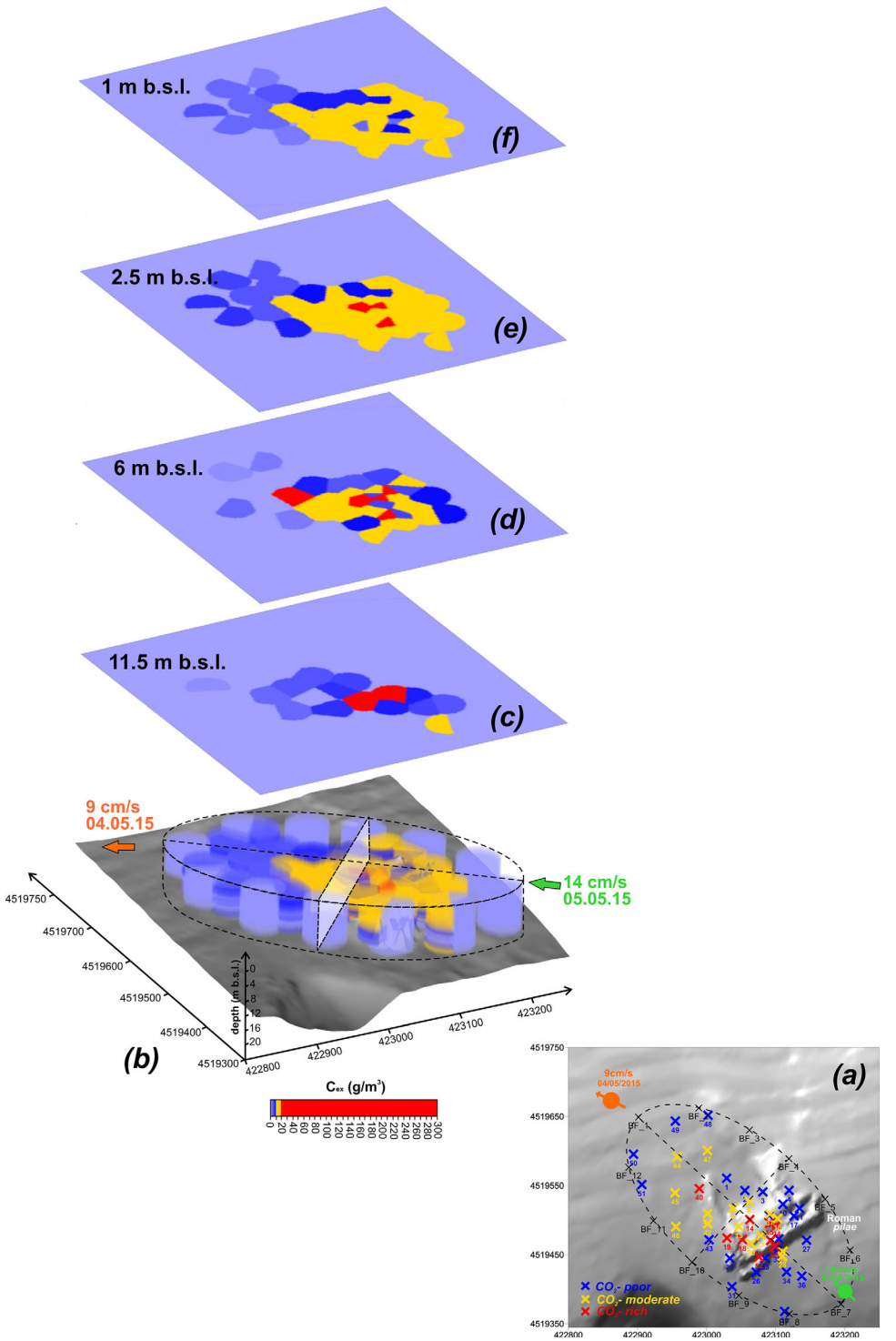

Figure 11. (a) Map showing the limits of the elliptic integration area (dashed line) used to calculate the total excess C mass ($C_{ex,TOT}$) in the SdF area. Black crosses are fictitious points (BF_1 to BF_12) with $C_{ex} = 0$ arbitrarily assigned along the entire seawater column. Green and orange symbols indicate the release positions and trajectories of drifters, that allow deriving the mean surface seawater currents in the two measurement days. (b) Volume rendering of C_{ex} resulting from the 3-D interpolation of 47 C_{ex} vertical profiles. The dashed squared surface cutting this volume represents the cross section perpendicular to the predominant seawater current direction (green and orange arrows), used for calculations of the C_{ex} flux ($\Phi C_{ex,TOT}$). (c–f) Orthogonal slices of the 3-D volume in Figure 11b, showing the C_{ex} spatial distribution at different depths (from 1 to 11.5 m b.s.l.) in the SdF area.

Taking all of these considerations into account, we finally interpret the N-S-trending fault-bounded depression (Figure 10) as the graben-like structure that formed during emplacement of the N-S-trending feeding dike of the Monte Nuovo eruption. The displacement of faults (both normal and reverse) suggests that dip-slip kinematics dominate, with subsidence in the central area. Graben-like structures are commonly formed during shallow dike emplacement, especially immediately before eruptions [*Trippanera et al*., 2015a, and references therein]. Their geometry is often complicated by local additional collapses (as occurred below the Monte Nuovo vent or, to a minor extent, SW of the SdF area; Figure 10), and by high-angle reverse faults to the sides. The latter are consistent with a graben-like structure considering the substantial vertical motion that results at the intersection between uplifted areas to the sides of the dike, and the subsided area above the dike. High-angle reverse faults are therefore not associated with compression, but simply result from the different vertical movements of two contiguous blocks [*Mandl*, 1988]. Similar reverse faults have been seen above experimental dikes, and to the sides of grabens in nature [*Trippanera et al*., 2015b]. The presence of hydrothermal vents on the eastern side of the graben (*SdF* in Figure 10), where the reverse faults are also found, suggests greater deformation and permeability on this side of the structure.

We propose that the graben resulted from an-elastic deformation due to the dike becoming shallower immediately before the eruption. The progression of the observed deformation, from the offshore to the onshore sector may reflect vertical emplacement of the dike, first deforming the lower areas (offshore) and then the higher ones (onshore).

5.3. CO_2 Flux

The SdF area (Figure 1) is currently the strongest (known) submarine hydrothermal offshore manifestation of CFc volcano, with a multitude of hot, saline hydrothermal vents distributed over a narrow area covering 0.14 km^2. Our geochemical profiles in Figures 5c and 5d clearly indicate that thermal fluid seafloor venting in the SdF area impacts the distribution of pH and pCO_2 in the overlying seawater column. The release of hot, acidic CO_2-rich fluids (see Table 2 and Figure 8) on the seafloor produces a wide pH and pCO_2 anomaly in the seawater, that is centered in the SdF Roman pilae (Figures 6a and 6b). Our results also demonstrate a minor but measurable change in C speciation in the seawater column, as reflected by a relative increase in $CO_{2(aq)}$ in the proximity of the emission vents (Figures 7d–7f). This detected anomaly in the water column (Figure 6a) makes it possible for quantify for the first time the total CO_2 flux from the submarine hydrothermal SdF vents. Below we describe the steps in the procedure used to estimate this CO_2 flux.

First, we calculate, for each site, the distribution of total dissolved excess C (C_{ex}) in the seawater column (Table 1). This is achieved by subtracting the vertical C_{TOT} distribution at background site 1B (Figure 7a) from the vertical distribution of C_{TOT} calculated at each site (supporting information Table S1). As such, C_{ex} represents the fraction of dissolved C in excess to that in "normal ambient seawater" (in which C is essentially derived from air-seawater exchanges and/or biological processes) [*Robinson and Brink*, 2005], and which we propose originates from hydrothermal seafloor venting. Our calculated C_{ex} values range from 0 to 275 g/m^3 (Table 1), and their spatial distribution mimics the pCO_2 distribution (Figure 6a). C_{ex} values increase from *CO_2-poor* sites (from $\sim$0 to $\sim<$ 15 g/m^3) to *CO_2-moderate* ($\sim$20 g/m^3), and peak at *CO_2-rich* sites ($>$20 g/m^3 and up to 274 g/m^3; Table 1), particularly in the central part of the SdF area (sites 18, 32, 35, and 52; Figures 6a and 6b) and at depth of 10–12 m b.s.l.

Second, we derive the 3-D distribution of C_{ex} in the SdF area (Figure 11b) by 3-D interpolation of the 47 derived C_{ex} vertical profiles (sites 1–52 in Table 1). Our interpolation algorithm uses the inverse distance gridding method, in which the weight of each data point in the interpolation decreases with distance over the grid nodes. In order to restrict the interpolation to a realistic 3-D space, we introduce some fictitious points (BF_1 to BF_12; black crosses in Figure 11a) to which $C_{ex} = 0$ is arbitrarily assigned at any depth of the seawater column. The output of the 3-D interpolation is the volume rendering shown in Figure 11b which comprises voxels (volume pixels) that are each characterized by a specific position in 3-D space and C_{ex} value. Figures 11c–11f are horizontal slices (ortho-images) through the volume rendering that illustrate the two-dimensional distribution of C_{ex} at distinct depths (from 1 to 11.5 m b.s.l.). The C_{ex} anomalies appear strongest (20–257$g \cdot m^{-3}$) and most clustered at depths of 10.5–11.5 m (Figure11c), to become wider (but more dilute) higher in the water column (at 2.5–6.0 m b.s.l.; Figures 11d and 11e). Note that a diffuse but weak C_{ex} anomaly (10–20 $g \cdot m^{-3}$) is visible in the slice at 1 m b.s.l. (Figure 11f).

Third, we multiply the volume of each voxel (in m^3) in Figure 11b by its corresponding C_{ex} values (in g/m^3) and, by summing over the entire population of voxels, we obtain a total excess C mass ($C_{ex,TOT}$, in g) within the considered volume, which is a cylinder with an elliptic base (Figure 11b). This procedure yielded an estimated $C_{ex,TOT}$ value of $5.4 \cdot 10^6$ g.

Finally, we consider that the above $C_{ex,TOT}$ mass flows continuously at a rate that is controlled by seawater current speed (~10 cm/s; section 4.3) through a rectangular cross section (with a surface area of ~1270 m^2) perpendicular to the predominant seawater current direction (NW-SE; Figure 11b). These values yield a daily C_{ex} flux ($\Phi C_{ex,TOT}$) of $\sim 52 \pm 10$ tons/d ($\sim 0.55 \pm 0.11$ kg/s), which we consider to be representative of the total C flux from the SdF hydrothermal vents.

5.4. Temperature Versus C_{ex} and Thermal Output

We next tested the hypothesis that thermal fluid venting on the seafloor not only alters the seawater C budget but also produces a weak (but measurable) thermal anomaly in the seawater column. During our campaign, we observed consistent temperature vertical profiles at all of the measured sites (Figure 5a). The temperature in the shallowest few meters of the seawater column is highly heterogeneous, and decreases rapidly with depth due to seawater surface heating from the atmosphere (a typical process in spring). This effect becomes smaller at greater depths in the water column, and the seawater temperature versus depth (negative) dependences become manifestly less pronounced. A particularly interesting observation was that the seawater temperature close to the seafloor in the SdF area (at depths of 8–12.5 m b.s.l.) shows a slightly larger variability (range: 16–19°C) than in the overlying layers (e.g., 17.5–19°C at depths of 5–7 m b.s.l.) (Figure 5a). We hypothesize that this larger temperature variability is caused by the local input of hot fluids at the seafloor.

To investigate this idea, we calculated the average temperature and C_{ex} (see section 5.2) in a 3 m thick layer for each vertical profile, centered at a depth of 9 m b.s.l. (the horizontal gray band in Figure 5a) (note that extending this procedure to greater depths would decrease the number of useful profiles). The two parameters exhibit a weak positive correlation ($R^2 = 0.48$; Figure 12a), suggesting that venting of C-rich fluids on the seafloor leads to a slight (<1°C) temperature increase in the seawater column. The association between temperature and C_{ex} is further supported by the maps in Figures 12b and 12c, in which the two parameters exhibit consistent spatial distribution patterns.

The enthalpy/CO_2 ratio of the SdF thermal end-member is unfortunately poorly characterized; our results (Figure 8f) provide evidence that thermal fluids have at least partially lost their original dissolved gas content prior to sampling (section 4.4). However, we can use the temperature versus C_{ex} relation in Figure 12a to attempt an order-of-magnitude estimation of the thermal end-member enthalpy/CO_2 ratio. The best-fit regression line of Figure 12a crosses the $C_{ex} = 0$ condition at 16.7°C, a temperature that is consistent with the background temperature at a depth of 9 m b.s.l. (Figure 5a) at background site 1B (i.e., the temperature of the water not affected by the input of hot fluids). Starting from this value, we computed the expected temperature versus C_{ex} trends that would result from the addition of hydrothermal fluids with distinct enthalpy/CO_2 ratios. For example, fumarolic fluids similar to those discharged at Solfatara (Figure 1) are, at least in principle, suitable candidates for being the thermal end-member in the SdF area, since a chemical affinity of gas released at the two manifestations was demonstrated by *Vaselli et al*. [2011]. However, the Solfatara fluids are characterized by very high CO_2 contents (on average of ~400 g per kg of fluid) and, owing to their relatively low enthalpy/C ratio (5.2 kJ per gram of CO_2), their injection at the seafloor would cause a much weaker temperature anomaly than seen in our profiles (Figure 12a). In contrast, the observed temperature versus C_{ex} trend is more compatible with the input of a CO_2-poorer geothermal liquid having an enthalpy/CO_2 ratio of 75–375 kJ/g_{CO2} (see orange lines in Figure 12a). Considering an estimated equilibrium temperature (from the Na-K geothermometer) of 179°C (see section 4.4), such enthalpy/CO_2 ratios would correspond to an original CO_2 content of 2–10 g per kg of fluid, which is reasonable for geothermal liquids. Finally, the best-fit line to the temperature versus C_{ex} data (Figure 12a) corresponds to the trend that would be caused by seafloor venting of fluids with an enthalpy/CO_2 ratio of ~139 kJ/g_{CO2} (which corresponds to a CO_2 content of ~5.4 g/kg for a geothermal liquid at 179°C). We finally assess the thermal output from the SdF area at ~80 MW by multiplying the above enthalpy/CO_2 ratio (of ~139 kJ/g_{CO2}) by our estimated total CO_2 output of 52 tons/d (546 g/d) (section 5.2).

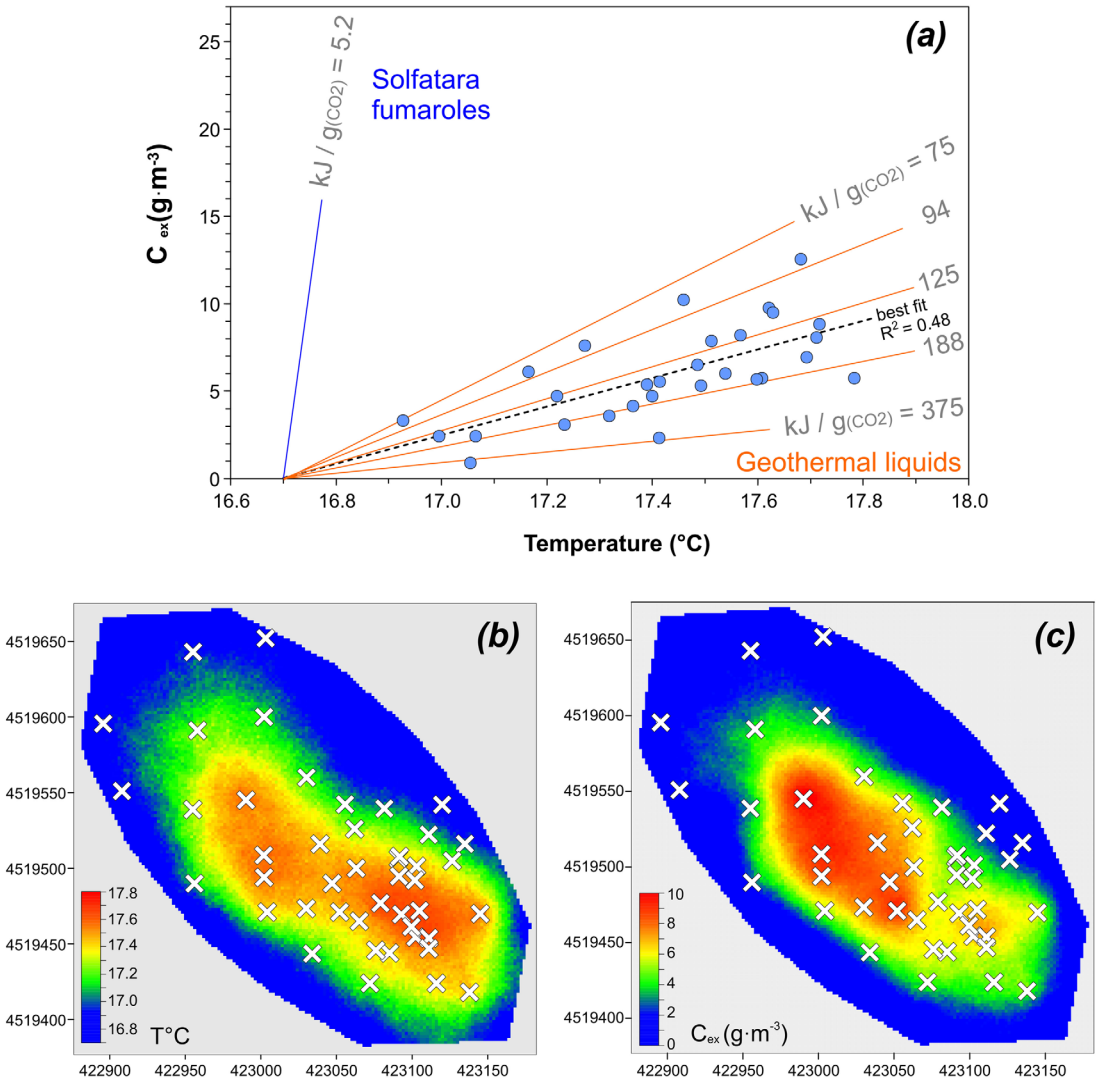

Figure 12. (a) Binary plot of average temperature versus C_{ex} in a 3 m-thick layer centered at a depth of 9 m b.s.l. along the water column in the SdF area. Blue and orange lines indicate the model-predicted temperature versus C relationship that would result from the addition of fluids with variable enthalpy/CO_2 ratios (see labelled values). (b and c) Maps of average temperature and C_{ex} in seawater, calculated in a 3 m-thick layer centered at a depth of 9 m b.s.l. (see gray band in Figure 5a). White crosses represent the locations of the seawater vertical profiles (as in Figure 1). The maps were realized by 100 sequential Gaussian simulations [*Deutsch and Journel*, 1998; *Cardellini et al*., 2003], based on an elliptic computational domain (same as in Figure 11a). At the border of the domain, we assumed background C_{ex} and temperature values of 0 g/m^3 and 16.7°C, respectively.

5.5. Implications for CFc

Our results reported here contribute new information that is relevant to the recent volcanological evolution and the present-day hydrothermal setting of CFc.

Our inferred deformation pattern for SdF and the Monte Nuovo sectors (Figure 10) provides new insights into mechanisms of shallow magma transfer underneath CFc. Our results suggest a N-S-oriented feeding dike for the Monte Nuovo eruption (Figure 10). This differs from the NNW-SSE-trending alignment of the two main vents of the eruption that have the clearest morphological expression. This slight difference in orientation suggests that it is more likely that the eruption was fed by a subcircumferential dike (concentric with the resurgent dome, and with the area of largest uplift in the recent decades) [*Acocella*, 2010; *Amoruso et al*., 2014; *Sacchi et al*., 2014], rather than a subradial dike, as apparently suggested by the NNW-SSE orientation. If this hypothesis is correct, this would imply that the feeder dike of the last CFc eruption propagated from the western sector of the shallow magmatic reservoir, and not from the caldera center. Confirmation of this inferred pre and syneruptive lateral shift of magmatic activity would have significant consequences for hazard assessment. It should warn about the possibility that the magma at CF may finally erupts at the

periphery of the area where long-term uplift (resurgence) [*Acocella*, 2010; *Sacchi et al*., 2014] and short-term uplift (unrest episodes during recent decades) [*Amoruso et al*., 2014; *D'Auria et al*., 2015] have been concentrated, such as in the center of the CFc where monitoring is currently focused.

Intensifying monitoring efforts on the western CFc sector is also strongly recommended based on our derived CO_2 and thermal outputs (sections 5.2 and 5.3). Our results indicate that the SdF area currently emits ~50 tons of CO_2 per day. This is only a small fraction (~3%) of the present-day CFc gas budget, which is dominated by CO_2-rich fumaroles and soils of the Solfatara-Pisciarelli degassing structure, in the caldera center (totally a daily CO_2 output of ~1600 tons equal to 16.8 kg/s) [*Chiodini et al*., 2010, 2012; *Aiuppa et al*., 2013]. However, the CO_2 flux at SdF remains substantial, falling within the range of those exhibited by recently active volcanic systems such as Poas (~20–55 tons/d equal to 0.21–0.58 kg/s) [*de Moor et al*., 2016], Hekla (~15 tons/d equal to 0.16 kg/s) [*Ilyinskaya et al*., 2015], or Soufrière of Guadeloupe (~15 tons/d equal to 0.16 kg/s) [*Allard et al*., 2014] (see also *Pedone et al*. [2014b] for an updated analysis of the global CO_2 flux distribution of quiescent hydrothermal volcanoes). The thermal output from the SdF area (80 MW) is even more significant, and close to that of the much larger (0.60 km^2) Solfatara-Pisciarelli degassing structure (~100 MW) [*Chiodini et al*., 2005]. In comparison, the energy release associated with hydrothermal diffuse degassing has been estimated to range from 0.9 to 42.6 MW [*Chiodini et al*., 2005], which is 2–80 lower than that at SdF. We therefore conclude that magma-sourced [*Vaselli et al*., 2011] leakage of gas and heat underneath CFc is not limited to the caldera center, but rather extends to its western margins.

6. Conclusions

Our multidisciplinary investigation has revealed novel aspects of a poorly studied offshore sector of CFc. We propose that the present-day morphology and structural setting of SdF was probably inherited from the last (AD 1538) CFc eruption at Monte Nuovo. This ridge-shaped submarine relief was modeled by high-angle faults formed to accommodate large vertical displacements at the eastern border of a graben system. We interpret this N-S-trending graben as the depression that opened in response to emplacement of the Monte Nuovo eruption feeding dike. This interpretation, if correct, implies that magma can be emplaced along subcircumferential fractures to the side of the magma chamber immediately before a CFc eruption. This means that the theatre of the next CF eruption might not correspond to the epicenter of the ground uplift currently being observed (at Pozzuoli).

Our measurements of the seawater pCO_2 and pH suggest that the SdF hydrothermal system contributes sizeable CO_2 (~50 tons/d, equal to 0.53 kg/s) and heat (~80 MW) outputs. Based on the chemistry of directly sampled seafloor vents, we attribute these relatively large gas and energy emissions to the venting of hot hydrothermal brines, with an enthalpy/CO_2 ratio of ~139 kJ/g CO_2, and deriving from a hydrothermal reservoir at ~179°C. The CO_2 output at SdF is equivalent to that of a typical quiescent volcano in the Solfatara activity stage (e.g., Soufrière de la Guadeloupe). The heat output is even more significant, corresponding to 80% of that currently contributed by the Solfatara-Pisciarelli degassing structure at the onshore CFc center. We therefore recommend that careful monitoring of temporal variations in the heat and CO_2 fluxes at SdF is necessary during the current period of CFc unrest.

Acknowledgments
This study was funded by the DPC-INGV Project V2 and by the European Research Council under the European Union's Seventh Framework Programme (FP7/2007/2013)/ERC grant agreement 305377. We wish to thank the Biosurvey staff (S. Calvo, C. Luzzu, and A. Scannavino) for logistical support during the October 2014 cruise on the Antonino Borzì R/V (www.biosurvey.it). The May 2015 campaign was carried out with assistance from staff (F. Saggiomo, A. Rignani) at Idrosfera (www.idrosfera.biz). We thank V. Pennino and E. Zizzo (University of Palermo) for help in seismostratigraphic and morphobathymetric data processing. Insightful comments by the Editor (Cin-Ty Lee), Tobias Fischer, and an anonymous Reviewer helped improving the manuscript. The authors have complied with AGU's data policy, and all of the available data are provided in tables and figures.

References

Acocella, V. (2010), Evaluating fracture patterns within a resurgent caldera: Campi Flegrei, Italy, *Bull. Volcanol.*, *72*, 623–638.
Acocella, V., and G. Chiodini (2015), Better forecasting for the next volcanic eruption, *Eos*, *96* (23), 11−15.
Aiello, G., A. Angelino, B. D'Argenio, E. Marsella, N. Pelosi, S. Ruggieri, and A. Siniscalchi (2005), Buried volcanic structures in the Gulf of Naples (Southern Tyrrhenian Sea, Italy) resulting from high resolution magnetic survey and seismic profiling, *Ann. Geophys.*, *48*(6), 883–897.
Aiuppa, A., G. Tamburello, R. Di Napoli, C. Cardellini, G. Chiodini, G. Giudice, F. Grassa, and M. Pedone (2013), First observations of the fumarolic gas output from a restless caldera: Implications for the current period of unrest (2005–2013) at Campi Flegrei, *Geochem. Geophys. Geosyst.*, *14*, 4153–4169, doi:10.1002/ggge.20261.
Aiuppa, A., L. Fiorani, S. Santoro, S. Parracino, M. Nuvoli, G. Chiodini, C. Minopoli, and G. Tamburello (2015), New ground-based lidar enables volcanic CO_2 flux measurements, *Sci. Rep.*, *5*, 1361, doi:10.1038/srep13614.
Allard, P., A. Aiuppa, F. Beatuducel, D. Gaudind, R. Di Napoli, S. Calabrese, F. Parello, O. Crispi, G. Hammouya, and G. Tamburello (2014), Steam and gas emission rate from La Soufriere volcano, Guadeloupe (Lesser Antilles): Implications for the magmatic supply during degassing unrest, *Chem. Geol.*, *384*, 76–93.
Amoruso, A., L. Crescentini, and I. Sabbetta (2014), Paired deformation sources of the Campi Flegrei caldera (Italy) required by recent (1980–2010) deformation history, *J. Geophys. Res. Solid Earth*, *119*, 858–887, doi:10.1002/2013JB010392.
Anwar, H. O. (1996), Velocity profile in shallow coastal water, *J. Hydraul. Eng.*, *122*(4), 220–223.

Baker, E. T., G. J. Massoth, C. E. J. de Ronde, J. E. Lupton, and B. I. A. McInnes (2002), Observations and sampling of an ongoing subsurface eruption of Kavachi volcano, Solomon Islands, May 2000, *Geology*, *30*, 975–978.

Barberi, F., D. P. Hill, F. Innocenti, G. Luongo, and M. Treuil (1984), The 1982–1984 bradyseismic crisis at Phlegrean Fields (Italy), *Bull. Volcanol.*, *47*(2), 173–411.

Bianco, F., E. Del Pezzo, G. Saccorotti, and G. Ventura (2004), The role of hydrothermal fluids in triggering the July-August 2000 seismic swarm at Campi Flegrei (Italy): Evidences from seismological and mesostructural data, *J. Volcanol. Geotherm. Res.*, *133*(1–4), 229–246.

Brandon, C., R. L. Hohlfelder, and J. P. Oleson (2008), The concrete construction of the Roman harbours of Baiae and Portus Iulius: The ROMACONS 2006 field season, *Int. J. Naut. Archaeol.*, *37*, 374–392.

Bruno, P. P. (2004), Structure and evolution of the Bay of Pozzuoli (Italy) by marine seismic data, *Bull. Volcanol.*, *66*, 342–355.

Butterfield, D. A., I. R. Jonasson, G. A. Massoth, R. A. Feely, K. K. Roe, R. E. Embley, J. F. Holden, R. E. McDuff, M. D. Lilley, and J. D. Delaney (1997), Seafloor eruptions and evolution of hydrothermal fluid chemistry, *Philos. Trans. R. Soc. London A*, *355*, 369–386.

Caliro, S., C. Panichi, and D. Stanzione (1998), Baseline study of the isotopic and chemical composition of waters associated with the Somma-Vesuvio volcanic system, *Acta Vulcanol.*, *10*, 19–25.

Caliro, S., G. Chiodini, R. Avino, C. Cardellini, and F. Frondini (2005), Volcanic degassing at Somma-Vesuvio (Italy) inferred by chemical and isotopic signatures of groundwater, *Appl. Geochem.*, *20*, 1060–1076.

Cardellini C, G. Chiodini, and F. Frondini (2003), Application of stochastic simulation to CO_2 flux from soil: Mapping and quantification of gas release, *J. Geophys. Res.*, *108*(B9), 2425, doi:10.1029/2002JB002165.

Chiodini, G., F. Frondini, C. Cardellini, D. Granieri, L. Marini, and G. Ventura (2001), CO_2 degassing and energy release at Solfatara Volcano, Campi Flegrei, Italy, *J. Geophys. Res.*, *106*, 16,213–16,221.

Chiodini, G., M. Todesco, S. Caliro, C. Del Gaudio, G. Macedonio, and M. Russo (2003), Magma degassing as a trigger of bradyseismic events: The case of Phlegrean Fields (Italy), *Geophys. Res. Lett.*, *30*(8), 1434, doi:10.1029/2002GL016790.

Chiodini, G., D. Granieri, R. Avino, S. Caliro, A. Costa, and C. Werner (2005), Carbon dioxide diffuse degassing and estimation of heat release from volcanic and hydrothermal systems, *J. Geophys. Res.*, *110*, B08204, doi:10.1029/2004JB003542.

Chiodini, G., S. Caliro, C. Cardellini, D. Granieri, R. Avino, A. Baldini, M. Donnini, and C. Minopoli (2010), Long-term variations of the Campi Flegrei, Italy, volcanic system as revealed by the monitoring of hydrothermal activity, *J. Geophys. Res.*, *115*, B03205, doi:10.1029/2008JB006258.

Chiodini, G., S. Caliro, P. De Martino, R. Avino, and F. Gherardi (2012), Early signals of new volcanic unrest at Campi Flegrei caldera? Insights from geochemical data and physical simulations, *Geology*, *40*, 943–946.

Chiodini G., J. Vandemeulebrouck, S. Caliro, L. D'Auria, P. De Martino, A. Mangiacapra, and Z. Petrillo (2015), Evidence of thermal-driven process triggering the 2005-2014 unrest at Campi Flegrei caldera, *Earth Planet. Sci. Lett.*, *414*, 58–67.

Cinque, A., G. Rolandi, and V. Zamparelli (1985), L'estensione dei depositi marini Olocenici nei Campi Flegrei in relazione alla vulcano-tettonica, *Boll. Soc. Geol. It.*, *104*, 327–348.

Coumou, D., T. Driesner, and C. Heinrich (2008), The structure and dynamics of mid-ocean ridge hydrothermal systems, *Science*, *321*, 1825–1828.

D'Auria, L., F. Giudicepietro, I. Aquino, G. Borriello, C. Del Gaudio, D. Lo Bascio, M. Martini, G. P. Ricciardi, P. Ricciolino, and C. Ricco (2011), Repeated fluid-transfer episodes as a mechanism for the recent dynamics of Campi Flegrei caldera (1989-2010), *J. Geophys. Res.*, *116*, B04313, doi:10.1029/2010JB007837.

D'Auria, L., F. Giudicepietro, M. Martini, and R. Lanari (2012), 4D imaging of the source of ground deformation at Campi Flegrei caldera (Southern Italy), *J. Geophys. Res.*, *117*, B08209, doi:10.1029/2012JB009181.

D'Auria, L., et al. (2015), Magma injection beneath the urban area of Naples: A new mechanism for the 2012–2013 volcanic unrest at Campi Flegrei caldera, *Sci. Rep.*, *5*, 1–15, doi:10.1038/srep13100.

de Moor, J.M., A. Aiuppa, J. Pacheco, G. Avard, C. Kern, M. Liuzzo, M. Martínez, G. Giudice, and T.P. Fischer (2016), Short-period volcanic gas precursors to phreatic eruptions: Insights from Poás Volcano, Costa Rica, *Earth Planet. Sci. Lett.*, *442*, 218–227, doi:10.1016/j.epsl.2016.02.056.

De Natale, G., C. Troise, F. Pingue, G. Mastrolorenzo, L. Pappalardo, M. Battaglia, and E. Boschi (2006), The Campi Flegrei Caldera, unrest mechanisms and hazards, *Geol. Soc. Spec. Publ.*, *269*, 25–45.

de Ronde, C. E. J., and V. K. Stucker (2015), Seafloor hydrothermal venting at volcanic arcs and back arcs, in *The Encyclopedia of Volcanoes*, 2nd ed., edited by H. Sigurdsson et al., pp. 823–848, Elsevier, Atlanta, Ga.

de Ronde, C. E. J., E. T. Baker, G. J. Massoth, J. E. Lupton, I. C. Wright, R. A. Feely, and R. G. Greene (2001), Intra-oceanic subduction-related hydrothermal venting, Kermadec volcanic arc, New Zealand, *Earth Planet. Sci. Lett.*, *193*, 359–369.

De Serio, F., and M. Mossa (2014), Streamwise velocity profiles in coastal currents, *Environ. Fluid. Mech.*, *14*, 895–918, doi:10.1007/s10652-014-9338-3.

De Siena, L., E. Del Pezzo, and F. Bianco (2010), Seismic attenuation imaging of Campi Flegrei: Evidence of gas reservoirs, hydrothermal basins, and feeding systems, *J. Geophys. Res.*, *115*, B09312, doi:10.1029/2009JB006938.

De Vivo, B., H.E. Belkin, M. Barbieri, W. Chelini, P. Lattanzi, A. Lima, and L. Tolomeo (1989), The Campi Flegrei (Italy) geothermal system: A fluid inclusion study of the Mofete and San Vito fields, *J. Volcanol. Geotherm. Res.*, *36*, 303–326.

Del Gaudio, C., I. Aquino, G.P. Ricciardi, C. Ricco, and R. Scandone (2010), Unrest episodes at Campi Flegrei: A reconstruction of vertical ground movements during 1905–2009, *J. Volcanol. Geotherm. Res.*, *195*(1), 48–56, doi:10.1016/j.jvolgeores.2010.05.014.

Deutsch, C. V., and A. G. Journel (1998), *GSLIB: Geostatistical Software Library and Users Guide*, 369 pp., Oxford Univ. Press, N. Y.

Di Fraia, G. (1993), Nuove evidenze topografiche e monumentali di Baia sommersa, in *Archaeologia Subacquea Studi*, *Ricerche*, documenti 1, edited by P. A. Gianfrotta and P. Pelagatti, vol.1, pp. 21–48, Ist. Poligrafico dello Stato, Roma.

Di Fraia, G. (2011), Un'isola scomparsa ed altre questioni baiane, in *Sibilla Cumana, la fonte del Sapere*, vol. 1, pp. 43–73, Iniziative Editoriali, Napoli.

Di Vito, M., L. Lirer, G. Mastrolorenzo, and G. Rolandi (1987), The 1538 Monte Nuovo eruption (Campi Flegrei, Italy), *Bull. Volcanol.*, *49*, 608–615.

Di Vito, M. A., R. Isaia, G. Orsi, J. Southon, S. de Vita, M. D'Antonio, L. Pappalardo, and M. Piochi (1999), Volcanism and deformation since 12000 years at the Campi Flegrei caldera (Italy), *J. Volcanol. Geotherm. Res.*, *91*(2–4), 221–246.

Di Vito, M. A., et al. (2016), Magma transfer at Campi Flegrei caldera (Italy) before the last 1538 A.D. eruption, *Sci. Rep.*, *6*, 32245, doi:10.1038/srep32245.

Dvorak, J.J., and P. Gasparini (1991), History of earthquakes and vertical ground movements in Campi Flegrei caldera, Southern Italy: A comparison of precursor events to the A.D. eruption of Monte Nuovo and of activity since 1968, *J. Geophys. Res.*, *48*, 77–72.

Ellis, A. J. (1971), Magnesium ion concentration in the presence of magnesium chlorite, calcite, carbon dioxide, quartz, *Am. J. Sci.*, *271*, 481–489.
Embley, R. W., C. E. J. DeRonde, S. G. Merle, B. Davey, and F. Caratori (2012), Detailed morphology and structure of an active submarine arc Caldera: Brothers volcano, Kermadec arc, *Econ. Geol.*, *107*, 1557–1570.
Fiedler, B., P. Fietzek, N. Vieira, P. Silva, H. C. Bittig, and A. Körtzinger (2013), In situ CO_2 and O_2 measurements on a profiling float, *J. Atmos. Oceanic Technol.*, *30*, 112–126.
Fietzek, P., B. Fiedler, T. Steinhoff, and A. Körtzinger (2014), In situ quality assessment of a novel underwater pCO_2 sensor based on membrane equilibration and NDIR Spectrometry, *J. Atmos. Oceanic Technol.*, *31*, 181–196, doi:10.1175/JTECH-D-13-00083.1.
Fofonoff, P., and R. C. Millard Jr. (1983), Algorithms for computation of fundamental properties of seawater, *Tech. Pap. Mar. Sci.*, 44, 53 pp., UNESCO, Paris, France.
Frankignoulle, M., and J. M. Bouquegneau (1990), Daily and yearly variations of total inorganic carbon in a productive coastal area, *Estuarine Coastal Shelf Sci.*, *30*, 79–89.
Giacomelli, L., and R. Scandone (2012), History of the exploitation of thermo-mineral resources in Campi Flegrei and Ischia, Italy, *J. Volcanol. Geotherm. Res.*, *209-210*, 19–32.
Giggenbach, W. F. (1988), Geothermal solute equilibria. Derivation of Na–K–Mg–Ca geoindicators, *Geochim. Cosmochim. Acta*, *52*, 2749–2765.
Guidoboni, E., and C. Ciuccarelli (2011), The Campi Flegrei caldera: Historical revision and new data on seismic crises, bradyseisms, the Monte Nuovo eruption and ensuing earthquakes (twelfth century 1582 AD), *Bull. Volcanol.*, *73*, 655–677, doi:10.1007/s00445-010-0430-3.
Hansen, P. J. (2002), Effect of high pH on the growth and survival of marine phytoplankton: Implications for species succession, *Aquat. Microb. Ecol.*, *28*, 279–288.
Ilyinskaya, E., A. Aiuppa, B. Bergsson, R. Di Napoli, T. Fridriksson, A. A. Óladóttir, F. Óskarsson, F. Grassa, M. A. Pfeffer, and K. Lechner (2015), Degassing regime of Hekla volcano 2012-2013, *Geochim. Cosmochim. Acta*, *159*, 80–99.
Isaia, R., P. Marianelli, and A. Sbrana (2009), Caldera unrest prior to intense volcanism in Campi Flegrei (Italy) at 4.0 ka B.P.: Implications for caldera dynamics and future eruptive scenarios, *Geophys. Res. Lett.*, *36*, L21303, doi:10.1029/2009GL040513.
Kerrison, P., J. M. Hall-Spencer, D. J. Suggett, L. J. Hepburn, and M. Steinke (2011), Assessment of pH variability at a coastal CO_2 vent for ocean acidification studies, *Estuarine Coastal Mar. Sci.*, *94*(2), 129–137.
Lambeck, K., F. Antonioli, M. Anzidei, L. Ferranti, G. Leoni, G. Scicchitano, and S. Silenzi (2011), Sea level change along Italian coast during Holocene and a projection for the future, *Quat. Int.*, *232*(1–2), 250–257, doi:10.1016/j.quaint.2010.04.026.
Lupton, J., M. Lilley, D. Butterfield, L. Evans, R. Embley, G. Massoth, B. Christenson, K. Nakamura, and M. Schmidt (2008), Venting of a separate CO_2-rich gas phase from submarine arc volcanoes: Examples from the Mariana and Tonga-Kermadec arcs, *J. Geophys. Res.*, *113*, B08S12, doi:10.1029/2007JB005467.
Mandl, G. (1988), *Mechanics of Tectonic Faulting: Models and Basic Concepts*, Elsevier, Amsterdam, Netherlands.
Marianelli, P., A. Sbrana, and M. Proto (2006), Magma chamber of the Campi Flegrei supervolcano at the time of eruption of the Campanian Ignimbrite, *Geology*, *34*, 937–940.
Marusic, I., B. J. Mckeon, P. Monkewit, H. M. Nagib, A. J. Smits, and K. R. Sreenivasan (2010), Wall bounded turbulent flows: Recent advances and key issues, *Phys. Fluids*, *22*, 065103.
Middelboe, A. L., and P. J. Hansen (2007), High pH in shallow-water macroalgal habitats, *Mar. Ecol. Prog. Ser.*, *338*, 107–117.
Millero, F. J. (1995), The thermodynamics of the carbonic acid system in the oceans, *Geochim. Cosmochim. Acta*, *59*, 661–667.
Miloshevich, L. M., A. Paukkunen, H. Vömel, and S. J. Oltmans (2004), Development and validation of a time-lag correction for Vaisala radiosonde humidity measurements, *J. Atmos. Oceanic Technol.*, *21*, 1305–1327.
Morhange, C., N. Marriner, J. Laborel, M. Todesco, and C. Oberlin (2006), Rapid sea-level movements and noneruptive crustal deformations in the Phlegrean Fields caldera, Italy, *Geology*, *34*, 93–96, doi:10.1130/G21894.1.
Nasello, C., and V. Armenio (2016), New small drifter for shallow water basins: Application to the study of surface currents in the Muggia Bay (Italy), *J. Sens.*, *2016*, 1–5, doi:10.1155/2016/6589636.
Nomikou, P., S. Careyc, D. Papanikolaoua, K. Croff Bellc, D. Sakellarioub, M. Alexandrib, and K. Bejeloua (2012), Submarine volcanoes of the Kolumbo volcanic zone NE of Santorini Caldera, Greece, *Global Planet. Change*, *90–91*, 135–151.
Okubo, C. H., and S. J. Martel (1998), Pit crater formation on Kilauea volcano, Hawaii, *J. Volcanol. Geotherm. Res.*, *86*, 1–18.
Orsi, G., M. D'Antonio, S. de Vita, and G. Gallo (1992), The Neapolitan Yellow Tuff, a large-magnitude trachytic phreato-plinian eruption: Eruptive dynamics, magma withdrawal and caldera collapse, *J. Volcanol. Geotherm. Res.*, *53*, 275–287.
Orsi, G., L. Civetta, M. D'Antonio, P. Di Girolamo, and M. Piochi, M. (1995), Step-filling and development of a three-layers magma chamber: The Neapolitan Yellow Tuff case history, *J. Volcanol. Geotherm. Res.*, *67*, 291–312.
Orsi, G., S. De Vita, and M. A. Di Vito (1996), The restless, resurgent Campi Flegrei nested caldera (Italy): Constraints on its evolution and configuration, *J. Volcanol. Geotherm. Res.*, *74*, 179–214.
Orsi, G., L. Civetta, C. Del Gaudio, S. de Vita, M. A. Di Vito, R. Isaia, S. M. Petrazzuoli, G. P. Ricciardi, and C. Ricco (1999), Short-term ground deformations and seismicity in the resurgent Campi Flegrei caldera (Italy): An example of active block-resurgence in a densely populated area, *J. Volcanol. Geotherm. Res.*, *91*(2–4), 415–451.
Orsi, G., M.A. Di Vito, J. Selva, and W. Marzocchi (2009), Long-term forecast of eruption style and size at Campi Flegrei caldera (Italy), *Earth Planet. Sci. Lett.*, *287*, 265–276, doi:10.1016/j.epsl.2009.08.013.
Pappalardo, L., L. Ottolini, and G. Mastrolorenzo (2008), The Campanian Ignimbrite, Southern Italy. geochemical zoning, insight on the generation of a super-eruption from catastrophic differentiation and fast withdrawal, *Contrib. Mineral. Petrol.*, *156*, 1–26.
Passaro, S., M. Barra, R. Saggiomo, S. Di Giacomo, A. Leotta, H. Uhlen, and S. Mazzola (2013), Multi-resolution morpho-bathymetric survey results at the Pozzuoli-Baia underwater archaeological site (Naples, Italy), *J. Archaeol. Sci.*, *40*(2), 1268–1278.
Pedone, M., A. Aiuppa, G. Giudice, F. Grassa, G. Chiodini, and M. Valenza (2014a), Volcanic CO_2 mapping and flux measurements at Campi Flegrei by Tunable Diode Laser absorption Spectroscopy, *Bull. Volcanol.*, *76*, 1209–1221, doi:10.1007/s00445-014-0812-z.
Pedone, M., A. Aiuppa, G. Giudice, F. Grassa, V. Francofonte, B. Bergsson, and E. Ilyinskaya (2014b), Tunable diode laser measurements of hydrothermal/volcanic CO_2, and implications for the global CO_2 budget, *Solid Earth*, *5*, 1209–1221, doi:10.5194/sed-5-1209-2014.
Pescatore, T., G. Diplomatico, M. R. Senatore, M. Tramutoli, and L. Mirabile (1984), Contributi allo studio de1 Golfo di Pozzuoli: Aspetti stratigrafici e strutturali, *Mem. Sot. Geol. Ital.*, *27*, 133–149.
Piochi, M., G. Mastrolorenzo, and L. Pappalardo (2005), Magma ascent and eruptive processes from textural and compositional features of Monte Nuovo pyroclastic products, Campi Flegrei, Italy, *Bull. Volcanol.*, *67*, 663–678, doi:10.1007/s00445-005-0410-1.

Robinson, A. R., and K. H. Brink (Eds.) (2005*)*, *The Global Coastal Ocean: Multiscale Interdisciplinary Processes, Vol. 13: The Sea*, 1033pp., Harvard Univ. Press, Cambridge, Mass.

Roche, O., B. van Wyk de Vries, and T.H. Druitt (2001) Sub-surface structures and collapse mechanisms of summit pit craters, *J. Volcanol. Geotherm. Res.*, *105*, 1–18.

Rosi, M., and A. Sbrana (1987), Phlegrean fields, *Quad. Ric. Sci., CNR*, *114*, 175 pp.

Rosi, M., A. Sbrana, and C. Principe (1983), The Phlegraean fields: Structural evolution, volcanic history and eruptive mechanisms, *J. Volcanol. Geotherm. Res.*, *17*, 273–288.

Rosi, M., L. Vezzoli, P. Aleotti, and M. De Censi (1996), Interaction between caldera collapse and eruptive dynamics during the Campanian Ignimbrite eruption, Phlegraean Fields, Italy, *Bull. Volcanol.*, *57*, 541–554.

Sacchi, M., F. Pepe, M. Corradino, D. Insinga, F. Molisso, and C. Lubritto (2014), The Neapolitan Yellow Tuff caldera offshore the Campi Flegrei: Stratal architecture and kinematic reconstruction during the last 15 ky, *Mar. Geol.*, *354*, 15–33.

Scognamiglio, E. (2002), Nuovi dati su Baia sommersa, *A. Subacq.*, *3*, 47–55.

Semesi, I.S., S. Beer, and M. Björk (2009), Seagrass photosynthesis controls rates of calcification and photosynthesis of calcareous macroalgae in a tropical seagrass meadow, *Mar. Ecol. Prog. Ser.*, *382*, 41–47, doi:10.3354/meps07973.

Somma, R., S. Iuliano, F. Matano, F. Molisso, S. Passaro, M. Sacchi, C. Troise, and G. De Natale (2016), High-resolution morpho-bathymetry of Pozzuoli Bay, southern Italy, *J. Maps*, *12*(2), 222–230, doi:10.1080/17445647.2014.1001800.

Staudigel, H., and D. A. Clague (2010), The geological history of deep sea volcanoes, *Oceanography*, *23*(1), 58–71.

Staudigel, H., A. A. P. Koppers, J. W. Lavelle, T. J. Pitcher, and T. M. Shank (2010), Mountains in the sea, *Oceanography*, *23*(1), 18–19.

Trippanera, D., V. Acocella, J. Ruch, and B. Abebe (2015a), Fault and graben growth along active magmatic divergent plate boundaries in Iceland and Ethiopia, *Tectonics*, *34*, 2318–2348, doi:10.1002/2015TC003991.

Trippanera, D., J. Ruch, V. Acocella, and E. Rivalta (2015b), Experiments of dike-induced deformation: Insights on the long-term evolution of divergent plate boundaries, *J. Geophys. Res. Solid Earth*, *120*, 6913–6942, doi:10.1002/2014JB011850.

Vanorio, T., J. Virieux, P. Capuano, and G. Russo (2005), Three dimensional seismic tomography from P wave and S wave microearthquake travel times and rock physics of the Campi Flegrei Caldera. *J. Geophys. Res.*, *110*, B03201, doi:10.1029/2004JB003102.

Vaselli, O., F. Tassi, D. Tedesco, J. R. Poreda, and A. Caprai (2011), Submarine and inland gas discharges from the Campi Flegrei (southern Italy) and Pozzuoli Bay: Geochemical clues for a common hydrothermal-magmatic source, *Procedia Earth Planet. Sci.*, *4*, 57–73.

Ventura, G., G. Vilardo, and V. Sepe (2009), Monitoring and structural significance of ground deformations at Campi Flegrei supervolcano (Italy) from the combined 2D and 3D analysis of PS-InSAR, geophysical, geological and structural data, *Final Programme and Proceedings of the 6th International Symposium on Digital Earth, 9–12 September 2009*, pp. 1–7, Beijing, China.

Weiss, R. F. (1974), Carbon dioxide in water and seawater: The solubility of a non-ideal gas, *Mar. Chem.*, *2*, 203–215.